

Universal Time effects on substorm growth phases and onsets

M. Lockwood¹

¹Department of Meteorology, University of Reading, Reading, Berkshire, RG6 6BB, UK

Key Points:

- 1 Universal Time (UT) effects in the magnetosphere are caused by the eccentric nature of Earth's intrinsic magnetic field
- 2 There is a UT dependence of the open flux (and hence also the integrated magnetopause reconnection voltage) needed to trigger substorm onset
- 3 Growth phases that lead to substorm onset show considerable preconditioning by prior reconnection

Corresponding author: Mike Lockwood, m.lockwood@reading.ac.uk

Abstract

Universal Time (UT) variations in many magnetospheric state indicators and indices have recently been reviewed by Lockwood and Milan (2023). Key effects are introduced into magnetospheric dynamics by the eccentric nature of Earth’s magnetic field, features that cannot be reproduced by a geocentric field model. This paper studies the UT variation in the occurrence of substorm onsets and uses a simple Monte-Carlo model to show how it can arise for an eccentric field model from the effect of the diurnal motions of Earth’s poles on the part of the geomagnetic tail where substorms are initiated. These motions are in any reference frame that has an X axis that points from the centre of the Earth to the centre of the Sun and are caused by Earth’s rotation. The premise behind the model is shown to be valid using a super-posed epoch study of the conditions leading up to onset. These studies also show the surprising degree of preconditioning ahead of the growth phase that is required, on average, for onset to occur. A key factor is the extent to which pole motions caused by Earth’s rotation influence the near-Earth tail at the relevant X coordinate. Numerical simulations by a global MHD model of the magnetosphere reveal the effect required to generate the observed UT variations and with right order of amplitude, albeit too small by a factor of about one third. Reasons why this discrepancy may have arisen for the simulations used are discussed.

Plain Language Summary

Earth’s magnetic field is eccentric in that the main magnetic (dipole) axis does not pass through the centre of the Earth. This introduces a wobble into many aspect of near-Earth space as Earth rotates. Many consequences of this have been noted in previous papers. This paper investigates the effect of the eccentricity on the phenomenon of magnetospheric substorms. It is shown that the explosive releases of energy stored in tail are more likely to start (“onset”) at some Universal Times (and therefore geographic longitudes) than others and an explanation of why is provided.

1 Introduction**1.1 Universal Time variations in the magnetosphere**

Lockwood and Milan (2023) have recently reviewed Universal Time (UT) variations in magnetospheric observations and indices. Their study included: the am planetary geomagnetic index (Mayaud, 1972; Lockwood et al., 2019); the SML auroral electrojet index (Newell & Gjerloev, 2011a, 2011b); the SMR partial ring current indices (Newell & Gjerloev, 2012); the polar cap indices (Stauning, 2007; Troshichev, 2022; Lockwood, 2023), transpolar voltage observations from Low-Earth Orbit (LEO) spacecraft (e.g., Hairston & Heelis, 1993; Boyle et al., 1997), Φ_{PC} ; field aligned-current maps derived from measurements by magnetometers on the Iridium LEO satellites by the AMPERE (Active Magnetosphere and Planetary Electrodynamics Response Experiment) project (Coxon et al., 2018); and substorm onset occurrence (Forsyth et al., 2015; Newell & Gjerloev, 2011a, 2011b). In addition, Lockwood et al. (2021) have modelled the UT variations in the am index and its hemispheric sub-indices an and as and Lockwood et al. (2023) have studied how UT variations in the magnetosphere-ionosphere-thermosphere coupled system influence the upper atmosphere Joule heating response to terrestrial Coronal Mass Ejection (CME) impacts.

UT effects arise in the coupled magnetosphere-ionosphere-thermosphere system because the Earth’s magnetic poles are offset from its rotational axis. The most commonly used model of the intrinsic field of Earth is a geocentric dipole, for which this offset is the same in the two hemispheres. This means effects of Earth’s rotation in the northern polar regions are equal and opposite to those in the southern polar regions and taking a global average means that many effects cancel and show no net UT variation. How-

61 ever, constraining Earth’s magnetic dipole axis pass through the centre of the Earth is
 62 only a useful approximation and eccentric dipole models show that this is not generally
 63 valid. The standard way of describing an eccentric dipole, introduced by (Bartels, 1936),
 64 is to use the first 8 coefficients that define a spherical harmonic expansion of the mag-
 65 netic scalar potential, such as the International Geomagnetic Reference Field IGRF (Thébault
 66 et al., 2015). This is compared to the first three used to define a centered dipole. In such
 67 models the “axial” poles (where the dipole axis threads the Earth surface) are offset from
 68 the rotational axis by different amounts in the two hemispheres and these magnetic poles
 69 are not separated by 180° in longitude as they are for a geocentric dipole. The eccen-
 70 tric dipole model of (Koochak & Fraser-Smith, 2017a) gives the latitudinal offset of the
 71 axial magnetic pole and the rotational pole of 8.23° in the northern hemisphere in 1980
 72 and this fell to 5.91° in 2015. On the other hand, the corresponding values in the south-
 73 ern hemisphere were 15.29° in 1980 and 14.59° in 2015. Hence the ratio of the South/North
 74 magnetic pole offsets has risen from 1.86 to 2.47 in just 35 years because the northern
 75 magnetic pole has migrated towards the rotational axis. The motion depends on the type
 76 of pole considered (there are “dip poles” where the field is vertical as well as geocentric
 77 and eccentric dipole poles) but the acceleration of the northern pole has increased in re-
 78 cent years and this is likely to continue; however, although the changes in the core-mantle
 79 boundary that have caused this are understood, it is not yet possible to predict future
 80 changes (Livermore et al., 2020). Many effects of the offset of the rotational and mag-
 81 netic poles in the two hemispheres that cancel for a geocentric dipole do not cancel for
 82 an eccentric one leaving net UT variations. Thus the recent changes in the Earth’s in-
 83 trinsic field mean that UT effects in the magnetosphere-ionosphere-thermosphere sys-
 84 tem are of increasing importance. There are a number of potential effects discussed in
 85 the following subsections.

86 1.2 Ionospheric conductivity effects

87 The most commonly-invoked effect of the offsets of the magnetic and rotational poles
 88 is that of the changes in ionospheric conductivity at given polar and auroral locations
 89 in geomagnetic coordinates. This is because of the changes in solar zenith angles χ at
 90 such locations, which modulates the solar-EUV-generated ionospheric conductivities. This
 91 effect has been invoked a great many times in the context of UT variations in geomag-
 92 netic activity (e.g. Lyatsky et al., 2001; Newell et al., 2002; Wang & Lühr, 2007). This
 93 mechanism applies to enhanced conductivity that is generated by solar EUV illumina-
 94 tion (Ridley et al., 2004) and the effects at a given geomagnetic location are ordered by
 95 time-of-year (here quantified by the fraction of a calendar year, F) and UT . However,
 96 conductivity is also enhanced by particle precipitation. This second source is ordered in
 97 magnetic coordinates and is highly variable in time (Carter et al., 2020). At certain places
 98 and times, the precipitation source is dominant over the EUV source (Kubota et al., 2017).
 99 Both EUV and precipitation effects show transient events, the former mainly due to so-
 100 lar flare effects and the latter associated with magnetospheric storms and substorms. In
 101 both cases, strong UT variations occur as the event evolves but the timing of the events
 102 are essentially random in the UT of their occurrence and so regular, systematic UT vari-
 103 ations are not seen. We have had well-established and well-used models of EUV-generated
 104 conductivity for several years (e.g., Brekke & Moen, 1993) but the variability, in time
 105 and space, of precipitation-induced conductivity has made the development of equiva-
 106 lent models for precipitation effects much more difficult and complex (Zhang et al., 2015;
 107 Carter et al., 2020).

108 The dependence of EUV-generated conductivity at given geomagnetic coordinates
 109 on solar zenith angle means there is a dependence on the dipole tilt angle δ with which
 110 the Earth’s magnetic axis is tipped towards the Sun. In the Solar Geocentric Ecliptic
 111 (GSE) frame, the X axis points from the center of the Earth towards the center of the
 112 Sun, the Z axis is the northward normal to the ecliptic and Y makes up the right hand
 113 set (and so is antiparallel to Earth’s orbital motion). In three dimensions, the Earth’s

114 magnetic dipole axis \vec{M} makes an angle ψ with the GSE Z -axis and we here define the
 115 dipole tilt angle δ to be the angle that the projection of $-\vec{M}$ onto the GSE XZ plane
 116 makes with the Z axis. (Note that this definition means that positive δ means that the
 117 northern magnetic pole is tilted towards the Sun and the southern away from it and neg-
 118 ative δ means the southern/northern pole is tilted towards/away from the Sun). Because
 119 Earth’s rotational axis is inclined at 23.44° with respect to the Z axis, this gives an an-
 120 nual contribution to the variation in δ of $\pm 23.44^\circ$ which depends on the fraction of the
 121 calendar year, F . The present paper considers data for 1985-2021, the middle of that in-
 122 terval being 2003. In that year, Earth’s geocentric dipole axis made an angle of 10.32°
 123 with the rotational axis which gives an additional diurnal variation in δ of this ampli-
 124 tude, making the total range in δ over the year of $\pm 33.76^\circ$. For an eccentric dipole, off-
 125 sets of the north and south magnetic poles in 2003 were 6.81° and 14.96° , respectively,
 126 which gives total ranges of δ of $\pm 30.25^\circ$ and $\pm 38.40^\circ$ for the north and south poles re-
 127 spectively.

128 Low values of $|\delta|$ form a characteristic pattern called the “McIntosh” or “equinoc-
 129 tial” pattern with F and UT . This pattern is also observed in geomagnetic activity, first
 130 reported by McIntosh (1959) and frequently discussed since (for example Berthelier, 1976;
 131 de La Sayette & Berthelier, 1996; Cliver et al., 2000; Lockwood, Owens, Barnard, Haines,
 132 et al., 2020; Lockwood, McWilliams, et al., 2020; Lockwood et al., 2021). The equinoc-
 133 tial pattern is most clearly seen in the am index, which responds primarily to the sub-
 134 storm current wedge (Menvielle & Berthelier, 1991). The reason why am is the optimum
 135 index for observing this pattern is that it has the most uniform F - UT response pattern
 136 of all geomagnetic indices because it is constructed using homogeneous rings of stations
 137 in both hemispheres with weighting function corrections to allow for any unavoidable lon-
 138 gitudinal inhomogeneities in the siting of stations due to oceans (Lockwood et al., 2019).

139 Low δ gives larger solar zenith angles χ at high latitudes which gives lower values
 140 in EUV-generated ionospheric conductivity (Moen & Brekke, 1993; Ridley et al., 2004).
 141 However, the conductivity pattern depends on δ and not $|\delta|$ and so it is not obvious how
 142 conductivities could generate an equinoctial pattern in geomagnetic activity. The pro-
 143 posal of Lyatsky et al. (2001) and Newell et al. (2002) is that global geomagnetic activ-
 144 ity is enhanced when the midnight sector of both auroral ovals, where substorms are ini-
 145 tiated, are in darkness at E-region heights (solar zenith angles χ greater than about 101°)
 146 and so have a lower conductivity, and this only occurs when $|\delta|$ is small. Alternatively,
 147 the conductivity variation with χ proposed by Nagatsuma (2004) has, due to slant path
 148 effects, a minimum at $\chi = 90^\circ$ (which would be more common at low $|\delta|$). However,
 149 this minimum is not present in the models and observations of Brekke and Moen (1993),
 150 Moen and Brekke (1993) and Ridley et al. (2004).

151 It should be noted that, as discussed in the following subsections, EUV-enhanced
 152 conductivities in polar regions is far from the only proposed mechanism by which the
 153 F - UT equinoctial pattern of $|\delta|$ can be imprinted on global geomagnetic activity.

154 1.3 Dipole tilt effects in the geomagnetic tail

155 The near-Earth tail is orientated with respect to the Earth’s magnetic axis whereas
 156 the mid-tail and far-tail regions are orientated with respect to the solar wind flow (with
 157 a small aberration due to Earth’s orbital motion). Consequently, between the near-Earth
 158 and the mid-tail regions the tail bends through the “hinge angle” which is very close to
 159 being the same as the dipole tilt angle δ . Hence this tail hinge angle also shows the equinoc-
 160 tial pattern.

161 Kivelson and Hughes (1990) proposed that the hinge angle plays a role in the sta-
 162 bility of the tail and the triggering of substorm onsets, an idea investigated further by
 163 a number of authors (Danilov et al., 2013; Kubyshkina et al., 2015, 2022; Korovinskiy
 164 et al., 2018). To fit the observations, substorm occurrence and strength (and hence also

165 global geomagnetic activity) would need to be enhanced when the hinge angle is small
 166 (i.e., when $|\delta|$ is small). A variant of this idea was proposed by Alexeev et al. (1996) and
 167 Ou et al. (2022) who suggested the dipole tilt effect was through a change in the prox-
 168 imity of the ring current and the closest auroral electrojet.

169 A different mechanism for generating the equinoctial pattern in the geomagnetic
 170 tail has been proposed by Lockwood, McWilliams, et al. (2020); Lockwood, Owens, Barnard,
 171 Watt, et al. (2020). This uses the fact that the dipole tilt influences how quickly open
 172 field lines are appended to the tail because of the shift with δ in the magnetic latitude
 173 of the magnetic reconnection site in the dayside magnetopause, as has been modelled in
 174 numerical MHD simulations (Park et al., 2006; Hoilijoki et al., 2014; Lockwood, Owens,
 175 Barnard, Watt, et al., 2020; Eggington et al., 2020) and also observed in satellite data
 176 (Trattner et al., 2012; Zhu et al., 2015; Kitamura et al., 2016). In the hemisphere in which
 177 the dipole axis is tipped toward the Sun ($\delta > 0$ for the northern hemisphere), open field
 178 lines take longer than those in the other hemisphere or for when $\delta = 0$: this is because
 179 they have further to travel and because, initially, the open field lines are moving under
 180 the magnetic curvature force against, rather than with, the magnetosheath flow. As a
 181 result, a larger fraction of the open flux threads the dayside magnetopause sunward of
 182 a given X in the tail in the hemisphere tipped towards the Sun (and hence a smaller frac-
 183 tion threads the tail lobe at that X). Numerical simulations show that the total field, in
 184 both lobes, is smaller for larger $|\delta|$ and so the magnetic shear across the cross-tail cur-
 185 rent sheet is greatest for $\delta = 0$ and this too yields an equinoctial F - UT pattern (Lockwood,
 186 Owens, Barnard, Watt, et al., 2020). This mechanism is supported by the observation
 187 that the equinoctial pattern is enhanced by solar wind dynamic pressure which also en-
 188 hances the magnetic shear across the near-Earth cross-tail current sheet by squeezing
 189 the near-Earth tail (Lockwood, McWilliams, et al., 2020; Lockwood, Owens, Barnard,
 190 Watt, et al., 2020).

191 **1.4 Ion-neutral momentum exchange**

192 There are other effects of the Earth’s dipole tilt. The dynamics of ionospheric plasma
 193 is ordered relative to the geomagnetic pole whereas the dynamics of the neutral thermo-
 194 spheric gas is ordered relative to the rotational pole. Both ion-neutral and electron-neutral
 195 collisions contribute to ionospheric conductivities, but ion-neutral collisions have an ad-
 196 ditional role in momentum exchange between the ionosphere and thermosphere (specif-
 197 ically ions because their greater mass means that they carry much greater momentum
 198 than electrons). As a result, plasma convection influences thermospheric winds which,
 199 in turn influence the deposition of energy because ion-neutral frictional heating depends
 200 on the vector difference between the velocities of ions and neutrals. Hence both the wind
 201 response and the effect on energy deposition depend on UT (see review in Wang et al.,
 202 2017). An important factor in these effects is temporal variability in the ionospheric con-
 203 vection because the greater number densities of neutrals atoms compared to ions, results
 204 in the response times of thermospheric winds to changes in ionospheric flow being larger
 205 than the response times of ionospheric flows to changes in magnetospheric dynamics (Lockwood
 206 et al., 1988; Zou et al., 2021). Förster and Cnossen (2013) noted that the hemispheric
 207 intrinsic magnetic field differences were probably more important for polar thermospheric
 208 neutral winds than ionospheric plasma convection but can still influence currents, con-
 209 vection and power dissipation rates in the upper atmosphere and have implications that
 210 have been invoked by Cnossen et al. (2012), Förster and Cnossen (2013) and Laundal
 211 et al. (2017).

212 **1.5 The Russell-McPherron effect**

213 The Russell-McPherron (R-M) effect (Russell & McPherron, 1973) is central to un-
 214 derstanding the semi-annual variation in geomagnetic activity. A review of the evidence
 215 for this mechanism and of its influence has recently been given by Lockwood, Owens,

216 Barnard, Haines, et al. (2020) and Lockwood, McWilliams, et al. (2020). The R-M ef-
 217 fect arises because the IMF is ordered, on average, in a solar frame (the Parker Spiral
 218 configuration) but coupling into the magnetosphere depends on its orientation relative
 219 to Earth’s magnetic dipole axis (in a frame such as Geocentric Solar Magnetospheric,
 220 GSM). The most appropriate solar frame is the Geocentric Solar Equatorial (GSEQ).
 221 The key effect is due to the Earth’s dipole tilt: this results in negative IMF $[B_Y]_{GSEQ}$
 222 giving a southward IMF component in GSM (hence enhancing solar wind-magnetosphere
 223 coupling) around the March equinox whereas around the September equinox it is posi-
 224 tive $[B_Y]_{GSEQ}$ that has this effect. Geomagnetic activity shows, very clearly and very
 225 strongly, this preference for high geomagnetic activity at one or other equinox, depend-
 226 ing on the polarity of the $[B_Y]_{GSEQ}$ component (Zhao & Zong, 2012; Lockwood, Owens,
 227 Barnard, Haines, et al., 2020; Lockwood, McWilliams, et al., 2020). This confirms the
 228 key importance of the R-M effect. The diurnal dipole tilt variation due to Earth’s ro-
 229 tation means that the September peak (for $[B_Y]_{GSEQ} > 0$) is at around 10hrs *UT* (with
 230 a minimum around 22 hrs *UT*) whereas the March peak (for $[B_Y]_{GSEQ} < 0$) is at around
 231 22 hrs *UT* (with a minimum around 10 hrs *UT*).

232 1.6 Other dipole tilt effects on magnetopause reconnection voltage

233 The R-M effect has a characteristic *F-UT* pattern which is quite different to the
 234 equinoctial pattern in $|\delta|$. Hence the R-M effect does not generate the equinoctial pat-
 235 tern. Another proposal to explain the observed equinoctial pattern in geomagnetic ac-
 236 tivity is that the magnetopause reconnection voltage Φ_D varies with the dipole tilt (Crooker
 237 & Siscoe, 1986; Russell et al., 2003). However, (Finch et al., 2008) analysed the *F-UT*
 238 patterns in data from a very large number of individual magnetometer stations and showed
 239 that the equinoctial pattern arises in the nightside auroral oval and that it was absent
 240 absent in data from dayside stations. Similarly, (Lockwood, Owens, Barnard, Haines,
 241 et al., 2020) and (Lockwood, McWilliams, et al., 2020) used the mid-latitude *a σ* indices,
 242 which cover 6-hour ranges in Magnetic Local Time (*MLT*) and showed the equinoctial
 243 pattern was strongest in the midnight sector but hardly detectable in the noon sector.
 244 This argues against the equinoctial pattern being generated by dipole tilt effects on day-
 245 side magnetopause coupling and the magnetopause reconnection voltage Φ_D . These re-
 246 sults strongly indicate that the equinoctial pattern in indices such as *am* is not consis-
 247 tent with dipole tilt modulation of the reconnection rate in the dayside magnetopause.
 248 However, this does not mean that such effects do not occur and numerical simulations
 249 by global MHD models have found dipole tilt modulation of the reconnection voltage and
 250 in cross-tail current sheet. This is discussed further in Section 6.

251 1.7 Inductive effect of pole motions

252 Recently another mechanism has been added to this list. This is, in effect, a dif-
 253 ferent manifestation of the effect of dipole tilt on the evolution of open flux tubes into
 254 the tail proposed by Lockwood, Owens, Barnard, Watt, et al. (2020) and that was dis-
 255 cussed in Section 1.3. Lockwood et al. (2021) have noted that models and observations
 256 show that the ionospheric polar caps and auroral ovals undergo almost the same diur-
 257 nal sunward and antisunward sequence of motion due to Earth’s rotation as the geomag-
 258 netic pole in a geocentric-solar frame (meaning any frame that has an X axis that points
 259 from the centre of the Earth to the centre of the Sun, such as GSE, GSM and GSEQ).
 260 At first sight the velocities of these motions appear negligible, being smaller than typ-
 261 ical solar wind flow speeds in the same frame by a factor of order 2×10^{-4} . However, the
 262 flow-transverse magnetic field is larger in the ionosphere than in interplanetary space by
 263 a factor that is typically 10^4 and hence in terms of electric fields and voltages the pole
 264 motions give values that are typically about half those in interplanetary space.

265 As demonstrated by (Kabin et al., 2004), the effect of dipole tilt on the location
 266 of the open-closed field line boundary is readily seen in simulations made by numerical,

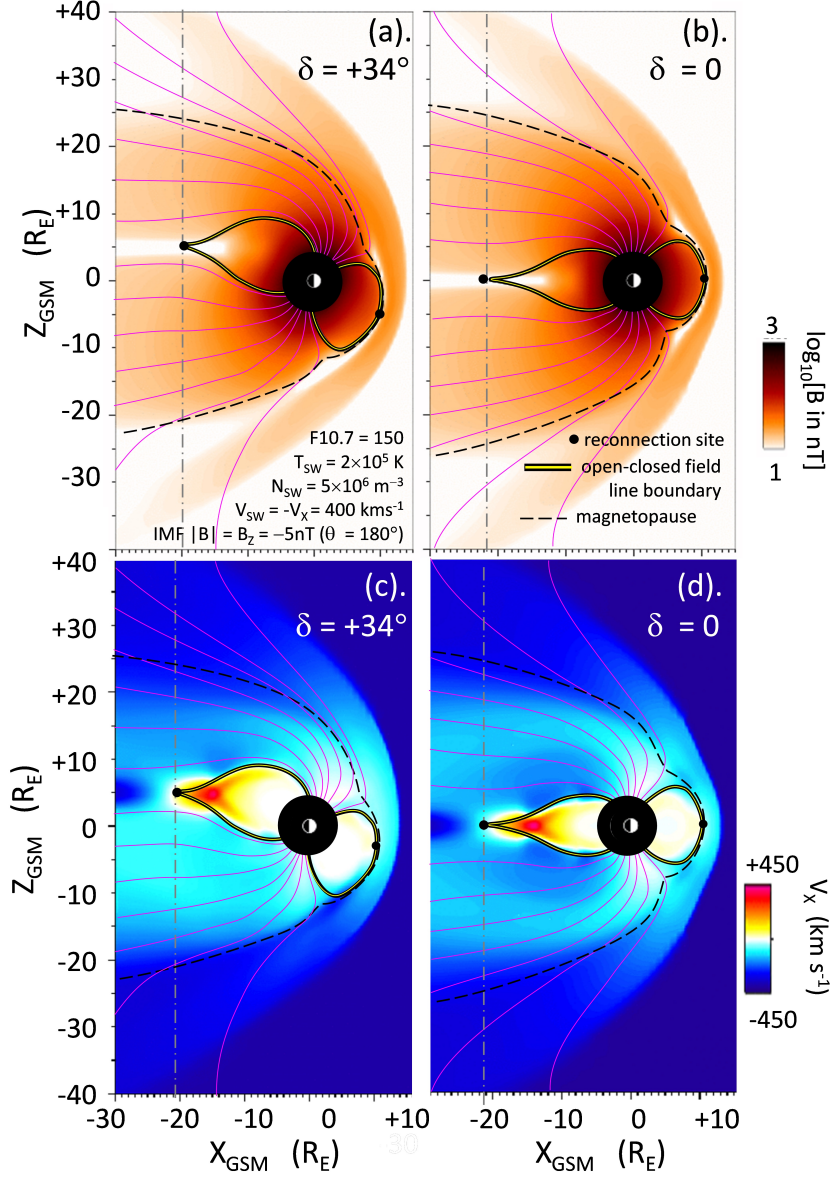


Figure 1. Numerical MHD model results from the SWMF model (version v20140611 - also known as BATSRUS) for run time 90 *min* in the simulations described by (Lockwood, Owens, Barnard, Watt, et al., 2020). Note these simulations use a geocentric dipole model of the Earth’s intrinsic field. The plots show noon-midnight cuts in the GSE XZ plane ($Y=0$), parts a and b give color contours of the magnetic field strength, B (on a logarithmic scale) and parts c and d give colour contours of the sunward flow speed, V_X . Parts a and c are for a dipole tilt of $\delta = +34^\circ$ and parts b and d are for $\delta = 0$. The magnetopause, defined from the plasma beta, flow and the magnetopause current in the Y direction, is shown as dashed lines and reconnection sites, identified by polarity flips in fast flows in the relevant direction, by black dots. The black and yellow line is the open-closed field line boundary. In addition, open magnetic field lines, reconnected 4 min apart, are shown in mauve. The vertical grey dot-dash line is at the X value of the tail reconnection X-line (at $Y=0$) which is at $X = -20.5 R_E$ for $\delta = +34^\circ$ and $X = -21 R_E$ for $\delta = 0$.

global, MHD models of the magnetosphere. Figure 1 shows simulations by the SWMF numerical MHD model (version v20140611, also known as BATSRUS) with a geocentric dipole model of the intrinsic geomagnetic field. The solar wind at (and before) the run time used here (90 min) was steady at 400km s^{-1} with an IMF pointing due southward in the GSM frame and of magnitude $5nT$. The solar wind number density was $3 \times 10^6\text{ m}^{-3}$ and the mean ion mass 1.1 amu. Using the empirical relation by Lockwood and McWilliams (2021a), the predicted magnetopause reconnection voltage Φ_D is constant at 56kV. Note that in order to isolate the effects of the dipole tilt angle δ , these simulations were carried out with two fixed values of δ (0 and 34°) and not one that varies with UT . Note also that the model has been run over 90 min to give a near steady-state with the effect of initial conditions removed.

Figure 1 shows noon-midnight cuts (i.e., in the XZ plane of the GSE frame) of the modelled structure in field strength (top panels) and antisunward flow speed (bottom panels) with the left-hand panels for a dipole tilt of $\delta = +34^\circ$ and the right-hand panels for $\delta = 0$. Plots for $\delta = -34^\circ$ are not shown because, for the geocentric dipole used, the results for the northern hemisphere are the same as for the southern for $\delta = +34^\circ$. The magnetopause is shown by the black dashed line and the X value of the tail reconnection site by the vertical grey dot-dash line. The mauve lines are open field lines that were reconnected 4 minutes apart. The symmetry of the $\delta = 0$ case means that the open field line motion into the tail is the same in the two hemispheres and Figure 1d shows that in both hemispheres open field lines have the same antisunward speed at the magnetopause at all X and that in both hemispheres open field lines take about 12.5 min for the point where they thread the magnetopause to reach the X coordinate of the tail reconnection site ($X \approx -21R_E$): as a result, in Parts b and d for both hemispheres the two most recently-reconnected field lines shown thread the magnetopause sunward of this X value, and the other 5 of the open field lines shown are appended to the tail lobe by this X : hence roughly $(5/7) \approx 70\%$ of the open flux is appended to both tail lobes at this X in this case.

Parts a and c of Figure 1 show how radically the dipole tilt alters this hemispheric symmetry. The field lines in the northern hemisphere reach a flow speed of $V_X = 200\text{km s}^{-1}$ at a GSE latitudes near 80° latitude (approximately 12 min after reconnection) whereas those in the southern hemisphere reach it at near 45° (after only 2.5 min). This is because the shift of the magnetopause reconnection site into the southern hemisphere means that for southern hemisphere open field lines the sheath flow and the tension force act together to move open flux tailward whereas initially the sheath flow is opposing the motion of northern hemisphere open flux towards the tail. As a result of this hemispheric difference in open flux evolution, only 4 out of the 7 open field lines are inside the tail lobe at the X of the tail reconnection site (approximately 60%) in the northern hemisphere, whereas in the southern hemisphere this figure is 6 out of 7 (approximately 86%).

The tilt of $\delta = 34^\circ$ used in Figure 1 is an extreme deviation from $\delta = 0$, slightly larger than the peak-to-peak diurnal variation of the southern ionospheric polar cap over 12 hours of 29.92° (for the pole offset in an eccentric dipole in 2003) and a bit over twice the corresponding diurnal range for the northern polar cap of 13.62° . However it clearly demonstrates how the polar caps move sunward and antisunward with the value of δ . The model runs shown in Figure 1 will be used in Section 5 to check that a best-fit value of a parameter used in this paper (R_X , defined in Section 2.1) is reasonable.

There is also diurnal motion of the ionospheric polar caps in the Y -direction, but this is different in the GSE, GSM and GSEQ frames as they differ in their Y -axis definition; however, they share the same X axis and so the polar cap motion in this direction (towards/away from the Sun) is the same in all these frames and here termed V_P (V_{PN} in the Northern hemisphere, V_{PS} in the southern). Assuming there is no change in the polar cap shape, the voltage across the polar cap generated by these pole motions in all three frames is

$$\phi = V_P B_i d_{PC} \quad (1)$$

where B_i is the ionospheric magnetic field and d_{PC} is the maximum diameter of the polar cap in the dawn-dusk direction, perpendicular to X. Note that d_{PC} , V_P and B_i are all values for the same altitude. We define V_P as positive for motion towards the Sun which is in the opposite direction to the solar wind flow (which is close to the $-X$ direction). For this definition, the voltage ϕ given by Equation 1 is subtracted from that generated across the polar cap by the solar wind flow because it is positive when the polar cap is moving sunward. Using the Expanding-Contracting polar cap model of ionospheric convection excitation (Cowley & Lockwood, 1992; S. E. Milan et al., 2021; Lockwood & McWilliams, 2021b; Lockwood & Cowley, 2022), the total voltage across the polar cap allowing for this pole motion effect becomes

$$\Phi_{PC} = f_D \Phi_D + f_N \Phi_N + \Phi_V - \phi \quad (2)$$

where Φ_D is the reconnection voltage in the subsolar dayside magnetopause (the rate of production of open flux), Φ_N is the reconnection voltage in the cross-tail current sheet that is between open flux in the tail lobes (the rate of loss of open flux), Φ_V is the “viscous-like” voltage induced by all non-reconnection mechanisms of solar wind-magnetosphere interaction. The factors f_D and f_N are the fractions of reconnection voltages (Φ_D and Φ_N , respectively) placed across the maximum diameter of the polar cap. These factors depend upon the shape of the polar cap and how it is changing: for the approximation of a polar cap that remains circular at all times $f_D = f_N = 0.5$ (Lockwood, 1993) but in general the polar cap boundary shape is always evolving (Tulegenov et al., 2023) and so the factors f_D and f_N are not constant.

It is worth noting that the Y-direction motion of the polar cap is likely to also have some effects, for example causing deformations of the ionospheric convection pattern, as illustrated schematically by Lockwood (1991). These diurnal motion of the polar cap would also be superimposed on the effect caused by the IMF Y-component described by Cowley et al. (1991) and are likely to add to the twist of the tail caused by IMF B_Y (Pitkänen et al., 2016) and hence the location of substorm onset (Østgaard et al., 2004), although some studies suggest such effects require a strong IMF B_Y that persists longer than the diurnal cycle of the pole motions (S. E. Milan et al., 2010). There are also indications that this can influence the occurrence of substorm onset (Liou et al., 2020).

Figure 2 looks at the implications of these pole motions by considering a Faraday loop PASGUC that is fixed in the GSM frame (shown by the yellow dashed line). The segment PC is the polar cap diameter and the voltage across (i.e. the magnetic flux transfer rate across it) is $\Phi_{PC} = V_i B_i d_{PC}$ where V_i is the plasma and frozen-in field velocity across it. The segment SG is just outside the bow shock in interplanetary space (sometimes referred to as the “Stern Gap”) and the voltage across it is $\Phi_{SG} = V_{SW} B_Z d_{SG}$, where V_{SW} is the solar wind speed in the $-X$ direction, B_Z is the interplanetary magnetic field (IMF) component in the GSM Z direction and d_{SG} is the spatial separation of S and G in the GSM Y direction (the width of the Stern gap). The segments of the loop PAS and GUC are the open field lines on the dawn and dusk extremities of the polar cap and neglecting any field-aligned voltages (that will be very small compared to Φ_{SG} and Φ_{PC}), Faraday’s law tells us the difference in the flux transfer rates $\Phi_{SG} - \Phi_{PC}$ is equal to the rate of growth of flux threading the loop PASGUC. Because the solar wind and relevant sheath flow are supersonic and super-Alfvénic, the solar wind flow and voltage Φ_{SG} is not influenced by any change in Φ_{PC} caused by the pole motion. Hence, in addition to reducing the transpolar voltage Φ_{PC} by ϕ , the effect of a sunward pole motion ($\phi > 0$) is to increase the lobe flux by ϕ .

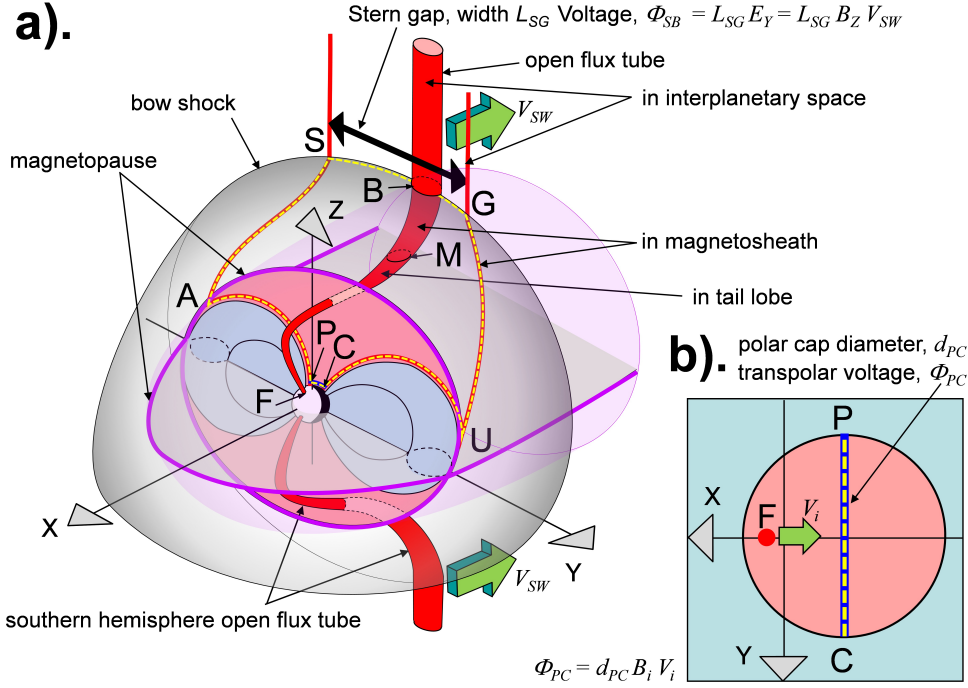


Figure 2. (a). Schematic of inductive decoupling of the “Stern Gap” voltage across open field lines in interplanetary space, Φ_{SG} and the transpolar voltage in the ionosphere Φ_{PC} . The magnetosphere is here viewed from northern middle latitudes in the mid-afternoon sector. The loops PASGUC (shown by the yellow dashed line) and PAUC (enclosing the northern tail lobe cross-section shaded pink) are fixed in the XYZ GSM frame, where P and C are the dawn and dusk extremes of the northern ionospheric polar cap, AP and UC are field-aligned in the magnetosphere, SA and GU are field-aligned in the magnetosheath, SG lies in the bow shock and AU in the tail magnetopause. The red flux tubes are open field lines and the northern-hemisphere tube threads the bow shock at B and the magnetopause at M and has an ionospheric footpoint, F. The solar wind flow is in the $-X$ direction at speed V_{SW} . (b) is a view looking down (in the $-Z$ direction) on the northern hemisphere polar cap in which the antisunward ionospheric convection velocity of the footpoint F is V_i . After Lockwood and Milan (2023).

366 Hence the diurnal cycle of sunward and then antisunward pole motion caused by
 367 the rotation of the Earth generates a diurnal cycle of decrease then increase of the iono-
 368 spheric transpolar voltage with an associated cycle of increase and then decrease in the
 369 rate at which open flux is added to the tail lobe.

370 1.8 Universal Time variations

371 Many of the effects discussed above generate systematic UT variations when a sub-
 372 set of the data are considered but not when averages of all data are considered. For ex-
 373 ample, the R-M effect generates UT variations if we consider the two polarities of the
 374 IMF separately, but because the distribution of IMF B_Y values is very close to symmet-
 375 ric around zero, the effects of the two polarities almost completely cancel in a full dataset
 376 and so the R-M effect does not give a net systematic UT variation if all data are con-
 377 sidered.

378 Indeed, because the dipole tilt angle averages to zero over a full year, this is true
 379 for any mechanism that depends linearly on the dipole tilt. However, EUV-induced iono-
 380 spheric conductivities have a non-linear dependence on solar zenith angle and hence on
 381 the dipole tilt. This means that the conductivity effects can give a net systematic UT
 382 variation even after averaging over a whole number of years. However, this depends on
 383 location, as demonstrated by Figure 6 of Lockwood and Milan (2023).

384 The pole-motion effect is different because the diurnal variation of the sunward ve-
 385 locities V_{PN} and V_{PS} are almost independent of the time of year (Lockwood et al., 2021)
 386 and so their diurnal effect is not reduced or eliminated by averaging over a whole num-
 387 ber of years.

388 Because the offset of the rotational and magnetic pole in the southern hemisphere
 389 is approximately twice that in the northern, the amplitude of the sinusoidal variation
 390 in the pole motion speed V_{PS} is approximately twice that in V_{PN} and so the effects on
 391 ionospheric transpolar voltage and lobe flux growth rate are roughly twice as large in
 392 the south than the north. In addition, whereas the sinusoidal variations would be in ex-
 393 act antiphase (and of equal amplitude) for a geocentric dipole model of the field (and
 394 hence would be equal and opposite and so cancel at any one time), the longitudinal sep-
 395 aration of the axial poles for an eccentric dipole is not 180° and the hemispheric vari-
 396 ations are not in exact antiphase as well as being different in amplitude. Thus there is
 397 a net UT variation for a global average for an eccentric dipole that is absent for a geo-
 398 centric dipole. The longitudinal separation of the poles from the Koochak and Fraser-
 399 Smith (2017b) eccentric dipole model has fallen from 152° in 1985 to 145° in 2015. This
 400 means that the phase difference between the sinusoidal variations in V_{PS} and V_{PN} has
 401 decreased from 0.85π to 0.81π , compared to the constant value of π for a geocentric dipole.

402 2 The effect of pole motions on substorm growth phases

403 2.1 A simple Monte-Carlo model of substorm growth phases and on- 404 sets

405 Lockwood and Milan (2023) have recently proposed a simple Monte-Carlo model
 406 of how pole motions influence substorm growth phases and so introduce a UT variation
 407 into substorm onset occurrence. This section refines that model slightly and Section 3
 408 provides an independent test of the concepts it is based on. In this model, the magne-
 409 topause reconnection voltage Φ_D is assumed constant and, because we are aiming to re-
 410 produce average behaviour, we use the overall average $\langle\Phi_D\rangle$ of 24 kV. In Lockwood and
 411 Milan (2023), the nightside reconnection voltage Φ_N was also held constant. In the present
 412 paper the linear open flux loss found by Lockwood et al. (2023) for times of small $|SML|$
 413 is used, with the loss time constant of $\tau_N = 6.8 \text{ hrs} = 2.448 \times 10^4 \text{ sec}$ reported in that
 414 paper. Thus the open flux continuity equation for the growth phases simulated is

$$dF_{PC}/dt = \Phi_D - \Phi_N = \Phi_D - F_{PC}/\tau_N \quad (3)$$

415 The questions then arise ‘when do growth phases end?’ and ‘what triggers substorm
 416 onset?’. This has been discussed for many years and many mechanisms proposed (Spence,
 417 1996; Lyons et al., 2018; S. E. Milan et al., 2019; Tanaka et al., 2021). To determine when
 418 onset occurs, the model uses the concept from the analysis of F_{PC} values at the time of
 419 onset by Boakes et al. (2009): this does not define the precise time of onset but does give
 420 us a usable statistical relationship. These authors found that for values of F_{PC} below
 421 0.3 GWb , the probability of a substorm onset occurring was negligible but that as F_{PC}
 422 rose above this level the probability increased linearly and was undefined above 0.9 GWb .
 423 Lockwood and Milan (2023) took the probability of onset to become unity at $F_{PC} = 1.2 \text{ GWb}$,
 424 the maximum possible open flux estimated by Mishin and Karavaev (2017). The impli-
 425 cation of the dependence of the probability of onset being set by the magnitude of the

426 open flux F_{PC} that it is set by the size of the cross-tail current (i.e., the magnetic shear
 427 between the two tail lobes) which increases with F_{PC} , at least at distances from the Earth
 428 small enough for solar wind dynamic pressure to cause the lobe fields to rise with increased
 429 F_{PC} . (Further down the tail, where the magnetopause becomes aligned with the solar
 430 wind flow, increased F_{PC} causes the tail to flare but the field in the lobe is set by the
 431 static pressure in the solar wind (Lockwood, 2013)). The flux in one tail lobe, $[F_{lobe}]_X$,
 432 at a given (negative) value of X in the tail, is given by

$$[F_{lobe}]_X = F_{PC} - F_X \quad (4)$$

433 where F_X is the open flux connected to the ionospheric polar cap in that hemisphere
 434 that still threads the dayside magnetopause sunward of X . Differentiating with time t
 435 gives

$$d[F_{lobe}]_X/dt = dF_{PC}/dt - dF_X/dt \quad (5)$$

436 The pole motion influence on F_X depends on the value of X considered and will
 437 decline with distance away from the Earth down the tail. We can allow for this with a
 438 factor that depends on X , R_X , which is the ratio $(dF_X/dt)/\phi$,

$$d[F_{lobe}]_X/dt = dF_{PC}/dt - R_X\phi \quad (6)$$

439 The factor R_X will, in general, depend on how much of the open flux was recently
 440 opened and hence the prior history of the voltage Φ_D . However, the constant Φ_D used
 441 in this simple model means that R_X will be constant for a given X . Substituting from
 442 equation 3 gives

$$d[F_{lobe}]_X/dt = \Phi_D - F_{PC}/\tau_N - R_X\phi \quad (7)$$

443 Note that Equation 7 applies to both hemispheres and that, because of Maxwell's
 444 equation $\nabla \cdot \vec{B} = 0$, Φ_D and F_{PC} are the same for both hemispheres, as is the loss time
 445 constant τ_N . On the other hand, we need to separately consider $(R_{XN}\phi_N)$ for the north-
 446 ern hemisphere and $(R_{XS}\phi_S)$ for the southern in order to compute the total tail lobe
 447 flux $[F_{tail}]_X$, which is the sum of the north and south lobe fluxes at X , $[F_{lobe}]_{XN}$ and
 448 $[F_{lobe}]_{XS}$:

$$d[F_{tail}]_X/dt = d[F_{lobe}]_{XN}/dt + d[F_{lobe}]_{XS}/dt = 2\Phi_D - 2F_{PC}/\tau_N - R_{XN}\phi_N - R_{XS}\phi_S \quad (8)$$

449 The survey by Boakes et al. (2009) found that substorm onset probability increased
 450 with the open flux F_{PC} . The model of substorm growth phases employed here uses the
 451 equivalent of the Boakes et al. (2009) result but also allows for the open magnetic flux
 452 that threads the dayside magnetopause, F_X and how it is influenced by the dipole tilt.
 453 It is proposed that the probability of onset being triggered primarily depends on the level
 454 of $[F_{tail}]_X$, rather than F_{PC} . In order to demonstrate the principle, the ratios R_{XS} and
 455 R_{XN} are taken to be equal and held constant. The value was varied and the optimum
 456 fit to the observed UT variation of substorm onset (see Section 2.3) was found for $(R_{XS} =$
 457 $R_{XN} = 0.15$ for the X coordinate relevant to substorm onset. In Section 3 this value
 458 is also shown to be consistent with a superposed epoch analysis of substorms onsets.

459 Because sequences of upstream IMF variation are independent of the phase of Earth's
 460 rotation, the model initiates each growth phase at a UT that is selected using a random

number generator. The integration of Equation 8 is started from an initial tail lobe flux (in each lobe) of $F_i = 0.2 \text{ GWb}$ ($[F_{tail}]_X = 0.4 \text{ GWb}$) which is consistent with typical quiet time values of F_{PC} . Note that, in reality, this value will vary but that lowering F_i increases the average length of the growth phases but does not influence the distribution of onset UT s because the start UT values of growth phases are randomly selected. Using equation 3, the value of F_{PC} throughout the growth phase is also computed and by assuming a circular polar cap this yields the polar cap diameter, d_{PC} (using the equation by Lockwood et al. (2023), based on the work of S. E. Milan et al. (2021)). This is used in Equation 1 to compute ϕ_N and ϕ_S at each time. The model calculates $[F_{tail}]_X$ every 1 second using Equation 8 and onset is determined to have occurred or not at each time step using a random number generator constrained to select onset occurrence based on the probability set by the $[F_{tail}]_X$ value. Note that there are three improvements in the model used here, compared to that used by Lockwood and Milan (2023): (1) it allows for the effect of growth in F_{PC} on the open flux loss rate Φ_N and (2) it allows for the effect of changing polar cap diameter d_{PC} on the pole-motion voltage ϕ (equation 1) and (3) it allows for the R_X factors.

This model is purely a model of substorm growth phases and onset and so cannot reproduce the intervals between onsets, Δt_o , because they also include the durations of the subsequent expansion and recovery phases (or alternatively the period of driven reconnection as discussed by S. E. Milan et al. (2021)) and any interval of quiet (northward IMF) conditions between the substorms. Also notice that each substorm growth phase in the model starts from the same initial tail flux $2F_i$ and at a randomly-selected UT . Hence the model cannot account for recurrent substorms during periods of persistent southward IMF, where a growth phase of a substorm starts immediately after the recovery phase of the prior substorm.

2.2 Effects of pole motions on transpolar voltages and the accumulation of magnetic flux in the tail lobes

Figure 3b and 3d show idealised variations that give an indication of how the pole motions influence the transpolar voltage and the accumulation of lobe flux at the X relevant to onset. This plot is illustrative and for constant values of the reconnection voltages Φ_D and Φ_N . The value of Φ_N and of the polar cap diameter d_{PC} employed would apply for a polar cap flux of $F_{PC} = 0.54 \text{ GWb}$. The key point is that effects of the pole-motions in the two hemispheres are not of equal amplitude nor in perfect antiphase, as they would be for a geocentric dipole. As a result, there is a sinusoidal variation in both the average Φ_{PC} and the average $\Delta[F_{lobe}]_X$ which is the integral of $R_X\phi$ with time. Figure 3c is for steady-state ($\Phi_D = \Phi_N$) whereas Figure 3d is for a growing polar cap with $\Phi_D=24 \text{ kV}$ and $\Phi_N=22 \text{ kV}$. Figure 3d shows that, compared to the case without pole motions (the dashed black line), the net effect of the UT variations is to reduce the rate at which flux is added to the tail between $2.5 \text{ hrs } UT$ and $14.5 \text{ hrs } UT$ but to enhance it at all other UT s.

2.3 The UT distribution of substorm onsets

Figure 4a shows the histograms of the numbers of substorm onsets N_o in UT bins 0.5 hrs wide, derived for 1985-2020 (inclusive) from the *SML* index and using the algorithm by Forsyth et al. (2015) (hereafter FEA). The onset list by Newell and Gjerloev (2011a, 2011b) (hereafter N&G) gives a very similar variation. The total number of substorm onsets ΣN_o is 88439 for the FEA list and 62532 for the N&G list. Hence the FEA list includes more and smaller events that are not counted as distinct onsets in the N&G list. Despite this difference, the distribution in UT is similar in the two cases with a large peak near $12 \text{ hrs } UT$. This is broadly reproduced by the simple Monte-Carlo model, as shown by the mauve lines in Figure 4a. In the model, this occurs because the slowing of the rate of accumulation of tail lobe flux means that more simulated growth phases

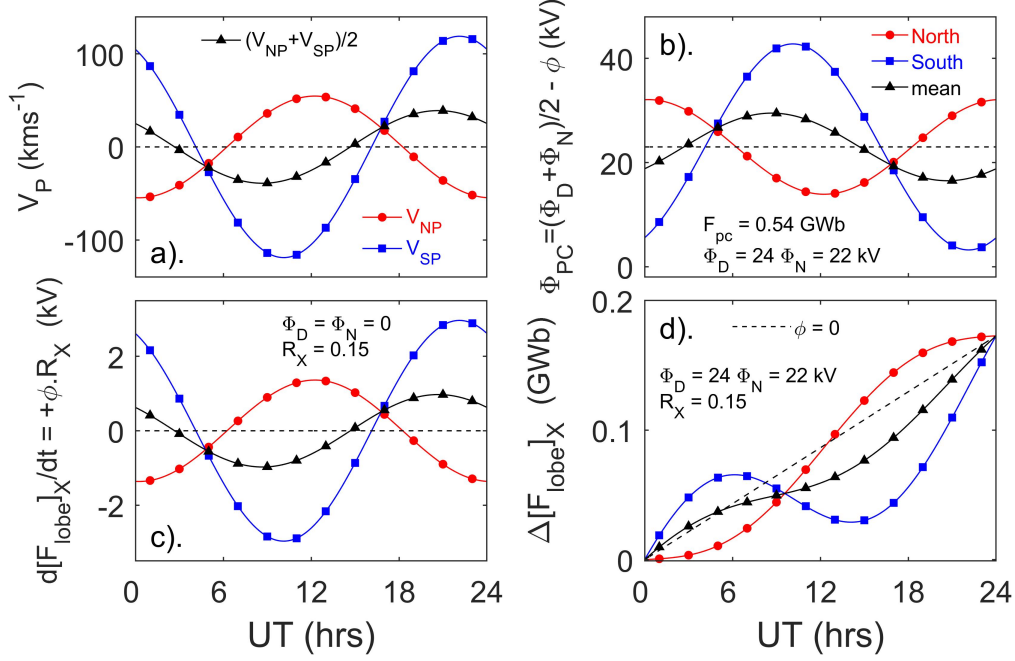


Figure 3. Plots of idealised Universal Time (UT) variations caused by pole motions. In all plots the red lines with red circle symbols are for the northern hemisphere polar cap, blue lines with blue square symbols are for the southern hemisphere polar cap and black lines with triangle symbols are for the global average of the two. Note that the symbols are added to aid readers with impaired colour vision and spaced considerably further apart than the UT resolution of the plots which is 1 min. Variations are based on the eccentric dipole model of Koochak and Fraser-Smith (2017b) for the year 2003. (a) the speed of sunward motion in the GSM frame of the geomagnetic poles at 120 km altitude in the E-region ionosphere, V_{NP} in the north, V_{SP} in the south and the average of the two in black. (b) The polar cap voltages Φ_{PC} from Equations 1 and 2 for constant dayside reconnection voltages of $\Phi_D = 24\text{ kV}$ and a constant nightside voltage of $\Phi_N = 22\text{ kV}$ (the value we would expect at low $-SML$ activity levels for an open flux of $F_{PC} = 0.54\text{ GWb}$ for the linear loss dependence with time constant $\tau_N = 6.8\text{ hrs}$). The viscous-like voltage Φ_V is set to zero. For a circular polar cap this F_{PC} gives a polar cap diameter of $d_{PC} = 3.71 \times 10^6\text{ m}$. (c) The contribution of the pole motions to the rate of accumulation tail lobe flux at X (for $R_X = 0.15$), $d[F_{lobe}]_X/dt = R_X \cdot \phi$ that would be the only change if steady state applied with $\Phi_D = \Phi_N$. (d) The total accumulation of lobe flux $\Delta[F_{lobe}]_X$ for the values of Φ_D, Φ_N in part (b). The dashed black line is for $\phi = 0$.

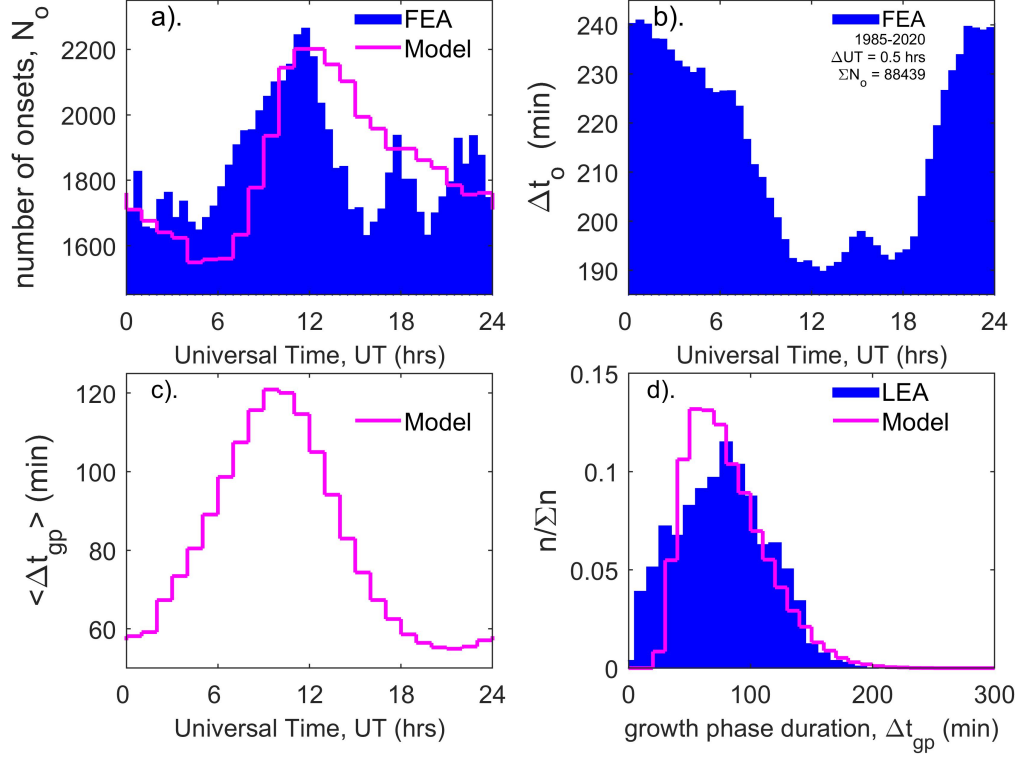


Figure 4. The blue histograms in the top panels show observed distributions with UT of (a) substorm onset times and (b) the interval after the prior onset from the list of such events compiled for 1985-2020 (inclusive) using the SML index and the algorithm by Forsyth et al. (2015). These plots both show a marked UT variation. The mauve line in (a) is the variation predicted by the simple Monte-Carlo model described in Section 2.1. (c) Means of the modelled growth phase duration in bins $\Delta UT = 1hr$ wide, $\langle \Delta t_{gp} \rangle$, as a function of UT . (d) The probability distribution of modelled growth phase durations Δt_{gp} (mauve line), where n is the number in bins $10min$ -wide bins and Σn is the total number (equal to 200,000 for the model simulations). Also shown by the blue histogram is the distribution for $\Sigma n = 368$ observed growth phase durations compiled by Li et al. (2013).

(that remember were started at randomly-chosen UT s) are reaching the required tail lobe flux to give a high probability of onset at those UT s. After 12 hrs UT the rate at which growth phases reach the onset threshold falls because the rate of increase in tail flux has grown. The observed mean time between onsets Δt_o is shown by the blue histogram in Part b: as discussed in Section 2.1, this cannot be reproduced by the model. Δt_o also shows a marked variation with UT : it decreases from near 4 hrs to close to 3 hrs over the interval 5-12 UT while the number of onsets N_o rises. However after 12 UT it remains low even though N_o falls again. This shows that although substorm onsets are rarer by 15 UT , the events that do occur tend to recur in short succession. As discussed in Section 2.1, this behaviour cannot be captured in the model which restarts each growth phase at a random UT and so it is not surprising the observed variation cannot be reproduced by the model at these UT s in Figure 4a. However, the model does explain how the dipole tilt effect gives the observed peak in onset occurrence at around 12 UT .

It is interesting to note what is happening in the growth-phase model. Initially the open flux F_{PC} is low and so the nightside reconnection voltage Φ_N is considerably smaller than the dayside voltage Φ_D . This means the polar cap flux grows rapidly. However, the rise in F_{PC} increases the value of Φ_N and the rise in F_{PC} slows. Eventually the difference between Φ_D and Φ_N becomes small and so the lobe flux variations due to the diurnal pole motions and, in particular, the variations that they cause in $[F_{lobe}]_X$ become significant. Hence although variations in $[F_{lobe}]_X$ due to the pole motions are small they have a significant impact on when the total tail field ($[F_{lobe}]_{XN} + [F_{lobe}]_{XS}$) reaches a value that makes the probability of an onset occurring high.

Figure 4c presents the UT variation in the mean of the modeled growth phase durations Δt_{gp} . Unfortunately, we do not have a large observational database to compare these predictions to. However, the plot confirms the above interpretation of the model predictions, with the growth phases coming to an end at around 12 UT having greater durations on average. Figure 4d shows the overall distribution of the 200,000 simulated Δt_{gp} values (in mauve) is quite similar to that of the 368 values observed by Li et al. (2013) (hereafter LEA), shown by the blue histogram. LEA divided the onsets into a high, medium and low subsets of the interplanetary electric field, E_{SW} , and showed that the distribution of Δt_{gp} values shifted to lower values for the larger E_{SW} cases, as we would expect. The distribution shown by the blue histogram in Figure 4d is the total for all three E_{SW} subsets. The mean value of the LEA distribution is 77 min which is close to the value of 81 min for the modelled distribution. The major difference is that the modelled distribution has fewer very short growth phases which suggests that either the initial total lobe flux F_i is slightly too low or that the threshold tail flux of 0.6 GWb for the probability of onset rising above zero is slightly too high.

3 Superposed epoch analysis of substorms

Section 2.3 shows that the simple Monte-Carlo model described in section 2.1, whilst not fully modelling the observed UT variation of substorm onsets, provides an important insight into dipole tilt effects. In this section we look for more direct evidence of such an effect using analysis of the variations in the SMU and SML geomagnetic indices and in the magnetopause reconnection voltage estimated from interplanetary measurements, Φ_D , using a superposed-epoch analysis (also known as Chree analysis or compositing). This paper presents the plots made using the FEA onset list, but results for the N&G list were similar.

Figure 5 presents superposed-epoch plots of the variations in (a) SML , (b) SMU and (c) Φ_D . The epoch time is relative to the times t_o of each of the 88439 substorm onsets in the FEA list for the years 1985 to 2020, inclusive. The mean value and the standard error in the mean are computed at epoch times $(t-t_o)$ between -240 min and +240 min in steps of $\delta t = 1$ min. This was repeated using randomly-selected epoch times t_o

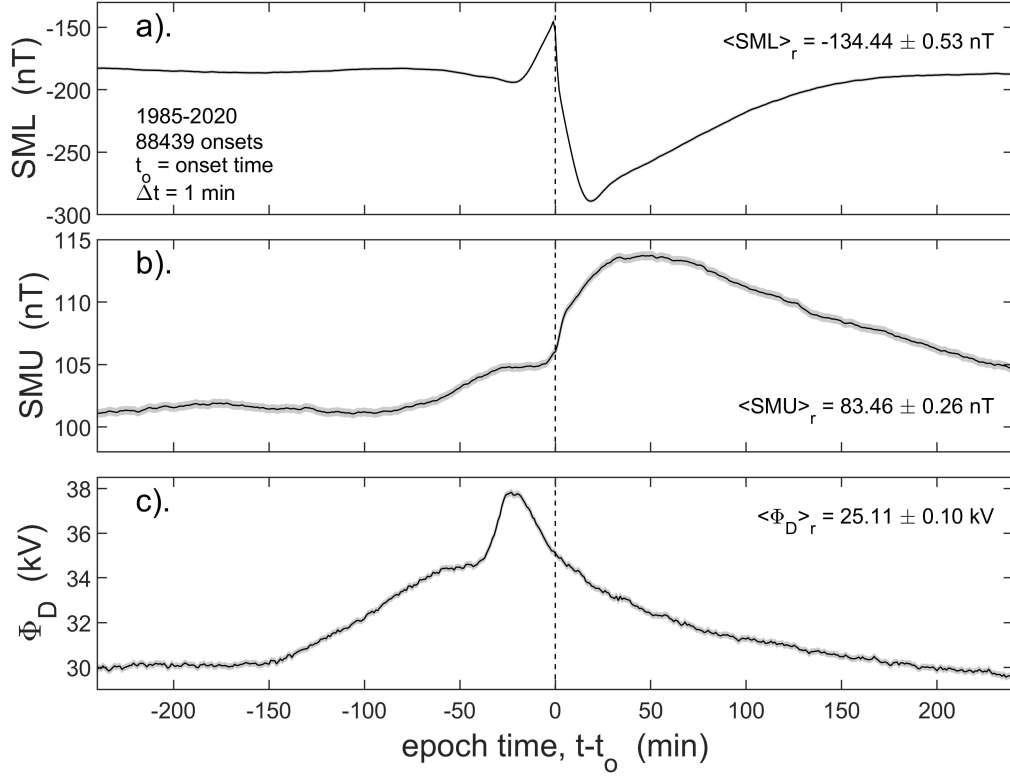


Figure 5. Superposed-epoch plots of substorms using the FEA list of substorm onsets for 1985-2020, inclusive. The mean value is shown as a function of epoch time ($t - t_o$), where t is the observation time and t_o is the time of onset, for: (a) the *SML* index; (b) the *SMU* index; and (c) the estimated reconnection voltage, Φ_D , lagged by a nominal propagation lag of $\delta t_p = 19$ min from the nose of the bow shock. The grey areas under the plotted black line are between plus and minus one standard error in the mean, but because of the very large number of samples (88439) these areas are smaller than the line width used for the case of *SML* and cannot be seen.

563 as a test of significance: because of the very large numbers of samples these random tests
 564 gave a completely flat variation: these are not shown in Figure 5 as values are consid-
 565 erably lower and so showing them suppresses detail in the plots for the real t_o ; however
 566 each plot gives the mean for the randomly-selected epoch times (respectively, $\langle SML \rangle_r$,
 567 $\langle SMU \rangle_r$ and $\langle \Phi_D \rangle_r$ in parts a, b and c), plus and minus the value of the mean of the
 568 corresponding standard errors. The randomly-selected onset values are shown in Figure
 569 8 which presents the superposed-epoch plots at lower time resolution but over consid-
 570 erably larger ranges of epoch time, $(t - t_o)$.

571 In Figure 5, the black lines are the mean values over-plotted on top of grey bands
 572 that are plus and minus the standard error in the mean. Because of the very large num-
 573 bers of samples, the gray band is hardly visible, especially for SML . The vertical black
 574 dashed line is at epoch time $(t - t_o) = 0$. The Φ_D data have been lagged by a nominal
 575 propagation lag of $\delta t_p = 19$ min from the nose of the bow shock. This value is appro-
 576 priate to the transpolar voltage Φ_{PC} and SML response to Φ_D (Lockwood & McWilliams,
 577 2021b), but values near 30-40 min would be more appropriate to the delay before sub-
 578 storm onset and SML . Hence in relation to onset the Φ_D curve in part c may need to
 579 be shifted to the left by an additional lag of about 10-20 min in some considerations.

580 The variation in SML in Figure 5a is as expected with some small changes in the
 581 growth phase shortly before onset and a big perturbation to large negative values start-
 582 ing at onset. It should be remembered the onset times are determined from SML and
 583 so we would expect SML to be well ordered by the onset times t_o derived from it. The
 584 variation in SMU is also as expected with small increases in the growth phase and then
 585 larger positive values after onset. Note that for the randomly-selected values of t_o the
 586 values (almost identical at all epoch times) are $\langle SML \rangle_r = -134.44 \pm 0.53$ nT and so larger
 587 (less negative) than for the real epoch times and values of $\langle SMU \rangle_r = 83.46 \pm 0.26$ are
 588 considerably lower. Hence in all of the 8 hours of epoch time shown, the disturbance lev-
 589 els of SML and SMU are considerably above the overall average values. Similarly $\langle \Phi_D \rangle_r$
 590 is 25.11 ± 0.10 kV at all epoch times and so considerably lower than for the 8 hour-period
 591 around substorm onset.

592 Figure 6 is the same as Figure 5c, but also shows the results for two one hour win-
 593 dows of the UT of the onset. The windows shown are 15-16 UT (in red) and 02-03 UT
 594 (in blue). These UT ranges are chosen as they give the maximum deviation either side
 595 of the values for all onsets. The means are taken over Δt of 5 min (rather than the 1 min
 596 used in Figure 5) because the higher time resolution is not needed and the 1-hour win-
 597 dows have fewer samples by a factor of roughly 24. The plot clearly shows that, on av-
 598 erage, larger Φ_D is needed ahead of substorm onsets at 15-16 UT than is needed ahead
 599 of onsets at 02-03 UT . The difference between the two is roughly constant at about 4
 600 kV at all negative values of $t - t_o$ shown and over that time this is a difference in opened
 601 flux of 0.058 GWb which is of order 10% of an average open polar cap flux, F_{PC} (S. E. Mi-
 602 lan et al., 2008; Boakes et al., 2009).

603 At the start and end of the period shown Φ_D is 30 kV (4.9 kV above average) and
 604 starts to rise above this at $t - t_o$ near -150 min. Thus the contribution of enhanced mag-
 605 netopause reconnection to the enhanced tail flux at onset, on average, begins at this time
 606 and increases until about 1 hour before onset (for the nominal propagation lag of $\delta t_p =$
 607 19 min). It then reaches a plateau for about half an hour before rising to a peak at $t -$
 608 $t_o = -25$ min (for the nominal $\delta t_p = 19$ min). This marks the southward turning of the
 609 IMF that is usually taken to be the start of the growth phase. However, the plot reveals
 610 two levels of “preconditioning” by enhanced Φ_D before this time. The first is the 4.9 kV
 611 by which Φ_D is elevated above average values 4 hours ahead of onset. The second is the
 612 reconnection taking place in the 2 hours before the inferred southward turning (between
 613 $t - t_o = -150$ min and $t - t_o = -30$ min on average). Thus the open flux gained only
 614 between the southward turning and onset is not the only contribution to the tail lobe
 615 flux at the time of onset.

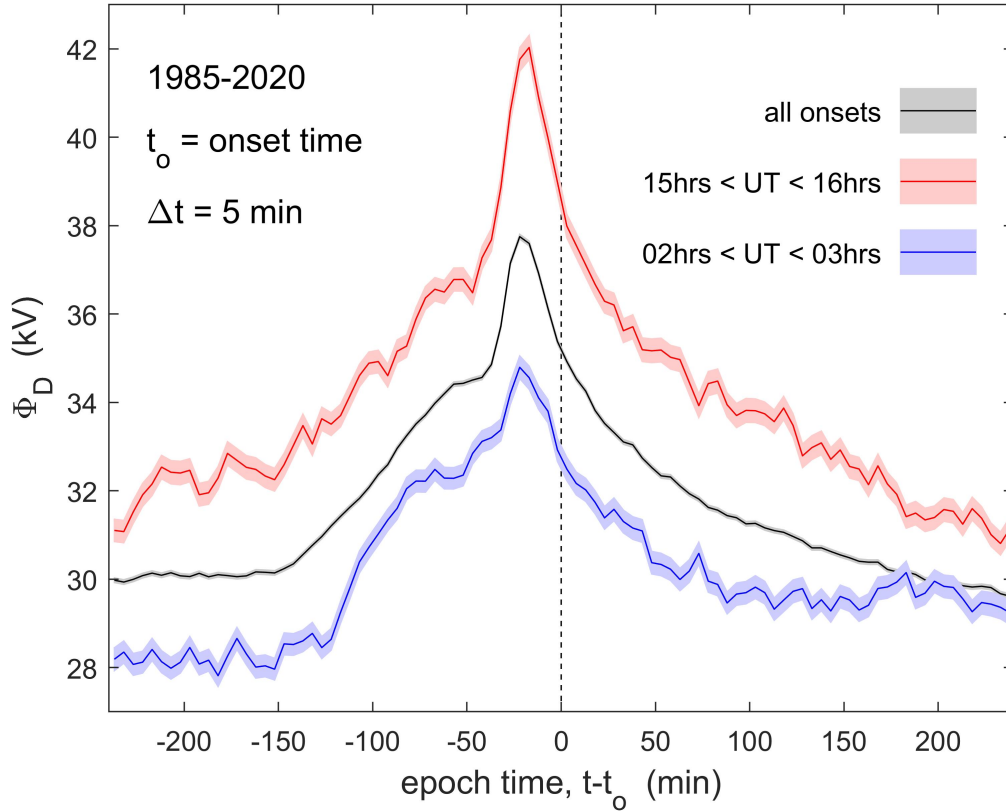


Figure 6. The same as Figure 5 but showing the values for onset UT between 15 and 16 hrs (in red) and between 02 and 03 hrs (in blue). The pink and pale blue shaded areas are plus and minus one standard error in the mean. The averages are here taken over $\Delta t = 5 \text{ min}$ windows in epoch time, $t - t_o$. The black line and grey shaded area is for all UT (also shown in Figure 5c).

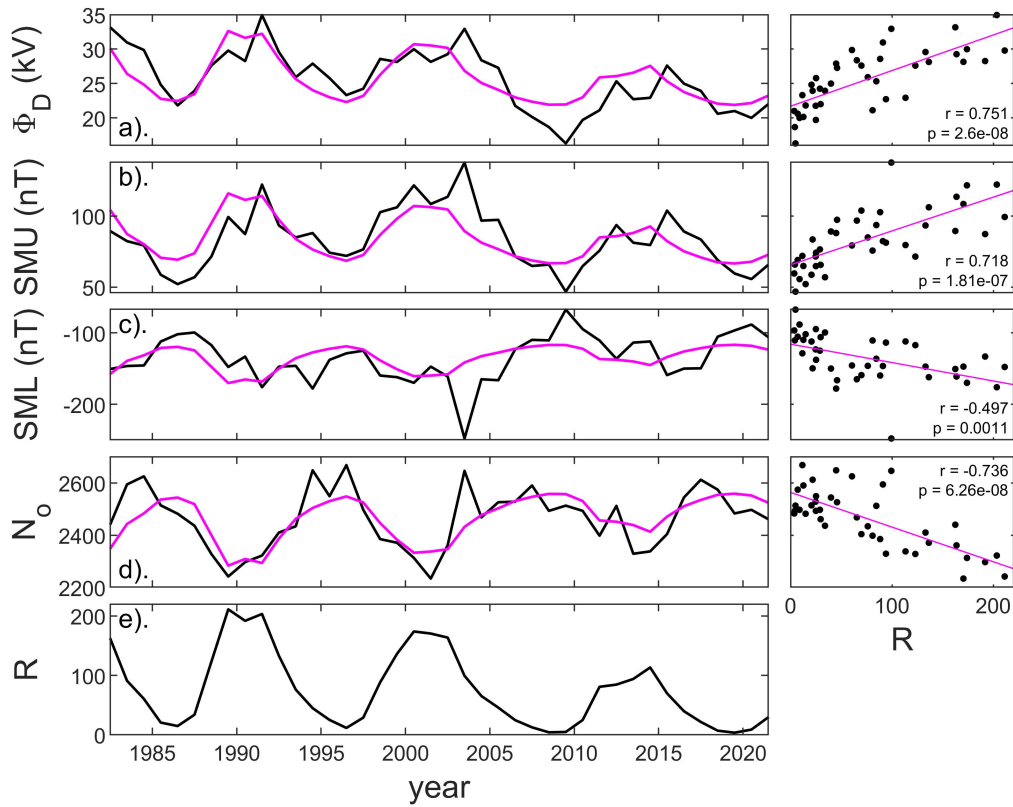


Figure 7. The left-hand column shows the Solar cycle variations in annual means (black lines) of: (a) the estimated magnetopause reconnection voltage, Φ_D ; (b) the *SMU* index; (c) the *SML* index; (d) the number of substorm onsets, N_o and (e) the international sunspot number, R . In panels a-d the mauve lines show the linear regression fit of R to the parameter. The right-hand column gives the scatter plots of the annual means with R , the mauve line being the linear regression fit. In each case, the correlation coefficient r and the p -value of the null hypothesis that there is no correlation are given.

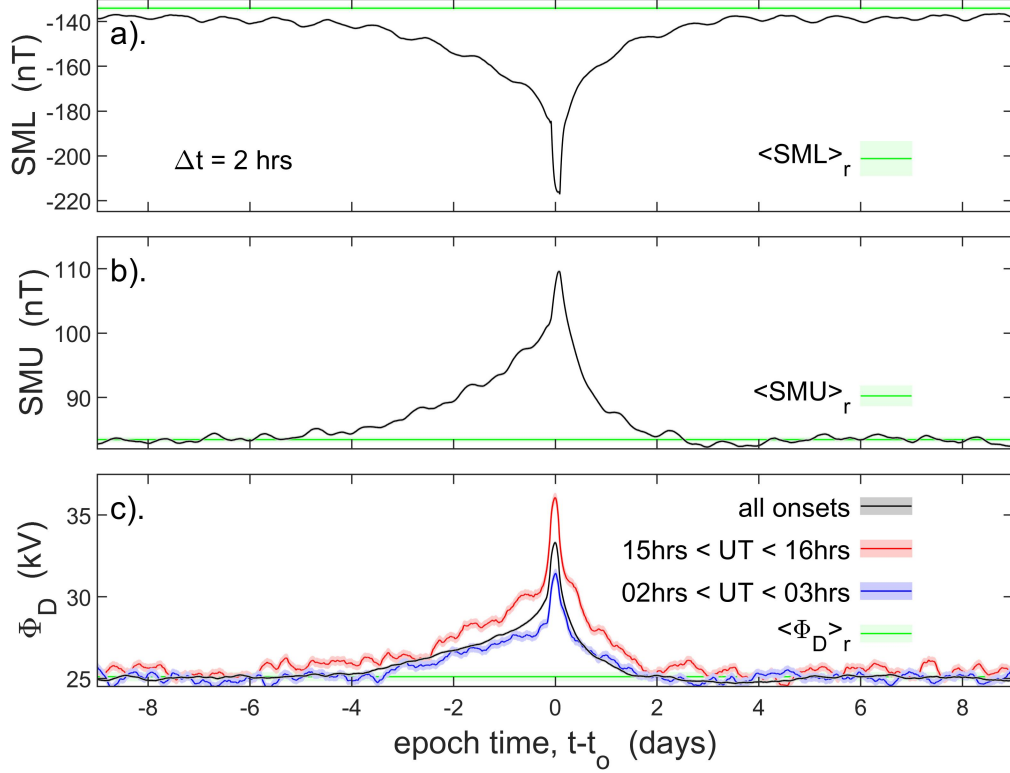


Figure 8. Super-posed epoch plots like those in Figures 5 and 6, but for integration intervals $\Delta t = 2$ hrs and covering epoch times ($t - t_o$) between -9days and +9 days, where t is the observation time and t_o is the time of onset, for: (a) the *SML* index; (b) the *SMU* index; and (c) the estimated reconnection voltage, Φ_D , lagged by a nominal propagation lag of $\delta t_p = 19$ min from the nose of the bow shock. The black lines are the means for all data and grey areas are plus and minus one standard error in the means. The green lines are for randomly selected epoch times. In Part c, the red and blue lines are means of Φ_D for onset *UT* between 15 and 16 hrs (in red) and between 02 and 03 hrs (in blue): the pink and pale blue shaded areas are plus and minus one standard error in the mean for these means.

616 The first preconditioning, seen as the 4.9 kV by which Φ_D is elevated at $t-t_o =$
 617 -240 min appears to be a solar cycle effect; however, Figure 7 shows that this is not the case.
 618 Such an effect would arise if onsets were more frequent at higher solar activity, as one
 619 might expect, and so the long-term averages of Φ_D , SMU and $-SML$ would all be increased
 620 above their overall means. Figure 7 plots the solar cycle variations in annual means for
 621 the dataset used here (1985-2021) and although Φ_D , SMU and $-SML$ are all correlated
 622 with sunspot number R as we would expect, surprisingly, the number of onsets per year,
 623 N_o is anticorrelated with more onsets occurring at sunspot minimum. (Note that SML
 624 not $-SML$ is plotted in Figure 7 and that the anticorrelation for SML is weaker than the
 625 other correlations (larger p value of the null hypothesis) largely because of the anomalous
 626 year 2003 for which the mean SML was exceptionally low).

627 On the anticorrelation of N_o and sunspot number, it is notable that (Tanskanen et
 628 al., 2011) found that full substorm cycles were most common in the declining phase of
 629 the solar cycle: hence their study gave a phase lag (relative to the sunspot cycle) of about
 630 $\pi/2$ for the number of full substorm cycles whereas the present study finds a phase lag
 631 of near π for the number of substorm onsets. S. E. Milan et al. (2021) show that 'driven
 632 convection' events occur when the dayside reconnection voltage Φ_D changes slowly enough
 633 for the nightside voltage Φ_N to respond and so the two can become balanced for extended
 634 periods in which no substorm cycles and no onsets occur. These events are what were
 635 termed 'steady convection events' by Lockwood et al. (2009) and McWilliams et al. (2008)
 636 showed that they are considerably more common at sunspot maximum than at sunspot
 637 minimum. This could therefore offer an explanation of the anti-correlation of N_o and sunspot
 638 number. However, this may also be convolved with the effect of high-speed solar wind
 639 streams that are more common in the declining and minimum phase of the cycle and have
 640 been observed to generate High-Intensity Long-Duration Continuous AE Activity (HILD-
 641 CAA) intervals in which substorm-like features merge into an interval of continuous substorm-
 642 like activity (Tsurutani et al., 2011; S. Milan et al., 2023): this could give more onsets
 643 at these cycle phases, as defined by the FEA and N&G algorithms.

644 Figure 7 shows that the enhanced Φ_D at the start of Figures 5 and 6 (over the over-
 645 all mean value which is very close to the value for random selection of epoch times be-
 646 cause the number of onsets is so high) is not due to the solar cycle variation in the num-
 647 bers of onsets. Figure 8 looks at the origin of this by extending the interval covered by
 648 the superposed epoch study and including the plots for the random selection of epoch
 649 times (the green lines with pale green areas showing plus and minus one standard error;
 650 however, in most cases these are smaller than the line width and not visible). In these
 651 plots the averaging interval was increased to $\Delta t = 2$ hrs. Part a shows that at epoch times
 652 well away from onset $t-t_o = -9$ days and $t-t_o = +9$ days, SML is very close to its over-
 653 all mean and the randomly sampled value $\langle SML \rangle_r$. Part b shows the same is true for
 654 SMU , the average value being found at $(t-t_o) < -5$ days and $(t-t_o) > +2.5$ days. The
 655 black line in part c shows that Φ_D is the same as its randomly-selected mean for $(t-t_o) < -5$
 656 days and that the variation for 15-16 UT is not elevated above that for 02-03
 657 UT for $(t-t_o) < -6$ days. Hence the UT variation in the voltage needed to cause an
 658 onset depends, to some degree, on a preconditioning (by prior magnetopause recon-
 659 nection) of the substorm growth phase over an interval of about 6 days before the south-
 660 ward turning that traditionally marks the start of the growth phase. The average effect
 661 of that preconditioning can be seen to increase considerably after $(t-t_o) = -2.5$ days.
 662 Magnetopause reconnection is likely to continue after onset and only at $(t-t_o) > 2$ days
 663 does the mean value of Φ_D fall back to its overall mean value. Hence substorm onsets tend
 664 to sit in intervals about 4.5 days long in which Φ_D is enhanced over the overall mean value.

665 The persistence in the plots in Figure 8 is surprisingly large. If we take the e-folding
 666 times to decay to e^{-1} times the peak for Φ_D at onset it is 0.99 days for going backwards
 667 with time before the peak and 0.42 days for after it. (For the 15-16 UT plot these e-folding
 668 times are 0.98 and 0.57 days, respectively, and for the 02-03 UT they are 1.11 and 0.46

669 days, and so very similar). Lockwood (2022) presented the autocorrelation functions for
 670 interplanetary parameters and for the various coupling functions derived from them. From
 671 these the correlation times (the e-folding times of the autocorrelation functions) are: 0.63
 672 days for the flow-transverse component of the IMF B_{\perp} , 2.43 days for the solar wind speed,
 673 $V_S W$; 0.57 days for the solar wind mass density ρ_{SW} ; and 0.07 days for the IMF ori-
 674 entation factor, $\sin^4(\theta/2)$ (where θ is the IMF clock angle in GSM). The value for Φ_D is
 675 0.17 days. Hence the decays either side in the peak in Figure 8c are longer-lived than
 676 the autocorrelation time of the Φ_D data series. However, Figure 8 is showing the aver-
 677 age of a great many cases. If we look at the variations around individual onsets at high
 678 time resolution they show frequent falls to near-zero Φ_D and then recoveries on typical
 679 variation timescale of about 0.05-0.1 days caused by the great variability in the IMF ori-
 680 entation factor. The greater persistence in the average of Φ_D for many cases arises be-
 681 cause the variability in the IMF orientation factor averages out to a near constant fac-
 682 tor and we see the greater persistence of the other parameters that contribute to Φ_D (in
 683 particular, the solar wind speed $V_S W$). Hence it is the relative longevity of the more-
 684 geoeffective fast solar wind streams that give the great persistence in the averages shown
 685 by the superposed epoch plots for Φ_D , SML and SMU in Figure 8.

686 It is interesting to note that integrating Φ_D over the interval between the appar-
 687 ent southward turning of the IMF (at $(t-t_o) = -35$ min, when mean values of Φ_D start
 688 to rise sharply to the pre-onset peak) and $(t-t_o) = 10$ min, we find a total of 0.1 GWb
 689 of open flux is generated. If we look at the total opened over the preconditioning inter-
 690 val -4 days $< (t-t_o) < -35$ min, it is 9.3 GWb. Much of this open flux will be lost and
 691 Figure 8a shows that average $-SML$ increases with the increasing Φ_D over this interval,
 692 indicating enhanced open flux loss by enhanced nightside reconnection. However it is in-
 693 teresting how little open flux is, on average, generated in the growth phase and how much
 694 the occurrence of a substorm onset relies on open flux accumulated during the precon-
 695 ditioning phase. The growth phase adds the final flux that triggers onset, but the role
 696 of prior open flux and preconditioning appears to be very significant.

697 3.1 UT variations in the reconnection voltage Φ_D prior to onset

698 The black line in Figure 9 shows the variation of mean open flux generated in the
 699 interval 150 min before onset to 10 min after, ΔF_{gp} , evaluated in bins of UT that are
 700 1 hr wide. This is surrounded by a grey area that is plus and minus one standard error
 701 in these means. Because the variations of average Φ_D with elapsed time $(t-t_o)$ are very
 702 similar in form for all UT s (as in Figure 6), the results are insensitive to the interval of
 703 elapsed times that is adopted. Indeed, the same form is even seen if we take the inte-
 704 gral over the whole preconditioning interval of 4 days before onset, as discussed above;
 705 however, just as the total fluxes opened in that longer interval are roughly ten times larger
 706 than in the hour before onset (as discussed in the previous section), so the amplitude
 707 of the UT variation is also ten times larger.

708 This plot shows that there is a significant UT variation in the flux that is opened
 709 ahead of substorm onsets. The mauve line (with an estimated error shown by the pink
 710 area) is the predicted variation for pole motion effect. This uses a value of R_X of 0.15
 711 in both hemispheres and was derived in Section 4 using the model used to predict the
 712 onset occurrence (see Figure 4a) and described in Section 2.1. The uncertainty of $\pm 20\%$
 713 that is derived in Section 5 from the numerical model predictions shown in Figure 1. It
 714 can be seen that this model prediction is not matching all the detail of the observed vari-
 715 ation, but both the phase and the amplitude of the main component is well reproduced.
 716 Hence the UT variations in both the occurrence of onset and the integrated reconnect-
 717 ion voltage needed to trigger a substorm can be predicted by the model based on the
 718 effect of pole motions.

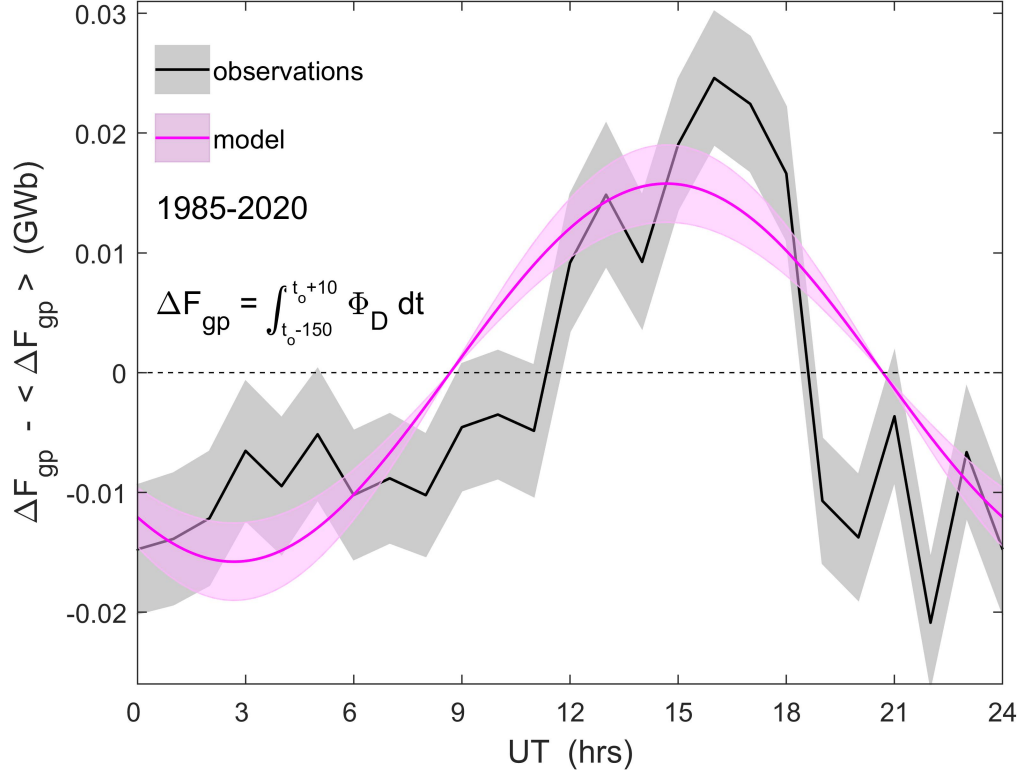


Figure 9. The variation of the open flux ΔF_{gp} generated in the substorm growth phase, taken to be the interval between 150 min before onset and 10 min after (using the nominal propagation lag of $\delta t_p = 19$ min from the nose of the bow shock), which is the integral of Φ_D over that interval. Values are shown as a function of UT for 1-hour intervals of UT and with the mean for all UT , $\langle \Delta F_{gp} \rangle$, subtracted. The black lines are mean values from the data, with the grey area showing plus and minus one standard error in the mean. The mauve line is the model prediction (see section 4) of text).

4 Analysis of UT variation of flux added in substorm growth phase

Figure 10a gives the changes in the lobe fluxes (at X near zero) caused by the motions of the poles, ΔF_{lobe} . This is the integral of the pole motion voltage ϕ with time. The colours and symbols are as used in Figure 3. Figure 10b is the variation of the lobe flux at $X = -21R_E$, $\Delta[F_{lobe}]_X$, obtained by multiplying the variations in Figure 10a by $R_X = 0.15$. The justification for this factor is discussed in the next section. The black line is the average of the two which will be half the UT variation of the total lobe flux in the tail, $\Delta[F_{tail}]_X$. The model assumes that it is this total flux that sets the probability of substorm onset occurring. To compensate for the UT variation in $\Delta[F_{tail}]_X$ and give the same probability of onset requires a UT variation in the total open flux produced by magnetopause reconnection which is given by the black line in Part c of Figure 10. This is the same variation as the black line in Part b, but inverted: it is the integral of the magnetopause reconnection voltage Φ_D needed, which has been derived from the superposed epoch analysis of the data in Section 3.1. The uncertainty band shown by the grey area is for a $\pm 20\%$ variation in R_X which is derived in the next Section 5.

The variation shown in Figure 10c is reproduced in Figure 9 as the mauve line with the uncertainty plotted in pink. It can be seen that the model is reproducing main phase and amplitude of the variation in prior reconnected flux with UT . The amplitude depends on value of $R-X$ of 0.15 which agrees with the simple Monte-Carlo model of onset occurrence and which, in the next section, is found to be a reasonable value using the numerical simulations which gave Figure 1.

5 Numerical modelling of the magnetotail response to dipole tilt

This section uses the results of a numerical, global, MHD model of the magnetosphere, shown in Figure 1, to gain some understanding of the factors R_{SX} and R_{NX} in Equation 8. The simulations are made using the BATSRUS global numerical model of the magnetosphere, specifically Space Weather Modeling Framework (SWMF) version v20140611 which deploys the RiceConvection Model. The runs were performed using NASA's Community Coordinated Modeling Center (CCMC) (Tóth et al., 2005) and the simulation results are described in the data availability section and were those used by Lockwood, Owens, Barnard, Watt, et al. (2020).

The simulations used are for tilt angles δ of 0, 34° and -34° . (Note that the use of a geocentric dipole field means that the third simulation for $\delta = -34^\circ$ gave identical results to $\delta = +34^\circ$ but with the north and south hemispheres reversed). All three simulations were started (at simulation time $t_s = 0$) with a large open flux of $F_{PC} = 0.85$ GWb which decayed until near steady state was achieved shortly after $t_s = 90$ min. The decay was greater for $\delta = \pm 34^\circ$ than for $\delta = 0$ largely because the dayside reconnection voltage Φ_D was persistently lower for $\delta = \pm 34^\circ$ and the nightside loss rate was high in both cases because F_{PC} was high. At simulation time $t_s = 90$ min, F_{PC} was 0.583 GWb for $\delta = 0$ and 0.509 GWb for $\delta = \pm 34^\circ$, a ratio of 1.145. For this time, the numerical simulations give Φ_D of 90.8 kV for $\delta = 0$ and 78.3 kV for $\delta = \pm 34^\circ$. These voltages were computed from the MHD simulation results using a variant of the method described by Laitinen et al. (2006). Specifically, the magnetopause location was defined from the abrupt change in plasma β and field lines at grid points on either side of this boundary traced in both directions using the tracing derived by the model. Field lines are then classified as A. disconnected (interplanetary only), B. open and connected to the south pole ionosphere, C. open and connected to the north pole ionosphere or D. closed (both ends connected to the ionosphere). Points between category B and C field lines and between category A and D field lines were identified as close to the reconnection X-line which was defined as the average of the midpoints between the pairs of opposing categories. These locations were then connected using PCHIP (Piecewise Cubic Hermite Interpolating Polynomial) interpolation of their X, Y and Z GSE coordinates and the electric field vari-

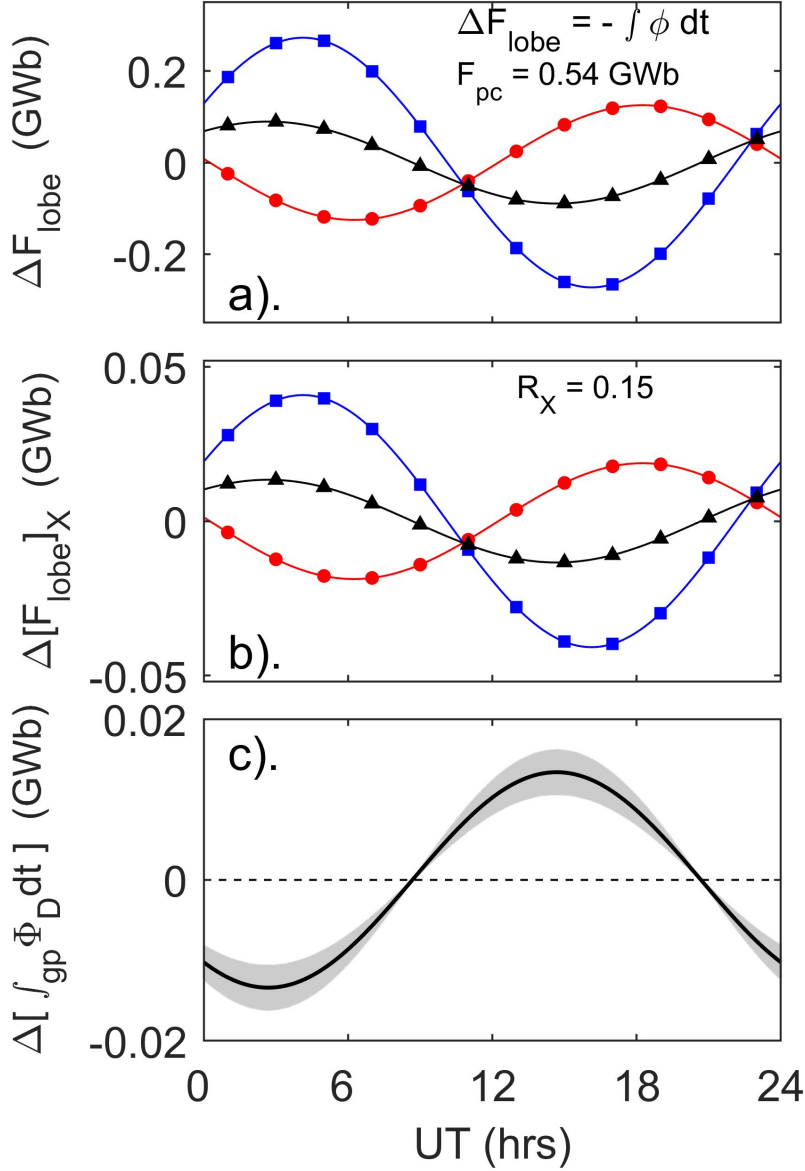


Figure 10. Variations giving the model prediction of the UT variation of flux opened during the growth phase, ΔF_{gp} shown in Figure 9. (a) the flux added to the lobes by the pole motions, ΔF_{lobe} , shown using the same colours and symbols as in Figure 3 (namely: red lines with red circle symbols are for the northern hemisphere polar cap, blue lines with blue square symbols are for the southern hemisphere polar cap and black lines with triangle symbols are for the global average of the two). This is the integral of ϕ with time for an average polar cap flux of F_{PC} of 0.54 GWb (giving a polar cap diameter d_{PC} of 3.73×10^6 m). (b) The variation in $[F_{lobe}]_X$, at a X coordinate of the tail reconnection site ($X = -21R_E$) (the same as inferred from the numerical simulation shown in Figure 1 and described below in Section 5). The value of R_X is 0.15, also used to make the model predictions in Figure 4. (c). The variation in the integrated growth phase reconnection voltage needed to offset the variation in the average tail $[F_{lobe}]_X$ caused by pole motions. This is an inversion of the black line in part (b). The uncertainty band shown in gray is derived in Section 5.

770 ation along this X-line also derived by PCHIP interpolation of nearby grid point values.
 771 When integrated along the X-line, these interpolated electric field (reconnection rate)
 772 values yield an estimate of Φ_D at that time.

773 The ratio of the reconnection voltages in the two cases was 1.160, similar to the
 774 ratio for F_{PC} . To allow for the different reconnection rates and make comparisons, all
 775 open magnetic fluxes are adjusted so that the F_{PC} is the average of the $\delta=34^\circ$ and $\delta=0$
 776 cases (i.e., 0.546 GWb) which means multiplying the open flux for $\delta=0$ by 0.937 and that
 777 for $\delta=\pm 34^\circ$ by 1.073. We also apply these factors to the two parts that add up to the
 778 total open flux (Equation 4), F_X and $[F_{lobe}]_X$. The analysis was repeated without these
 779 flux normalisation factors and the results for R_X were very similar because their effects
 780 on the fluxes F_X , ΔF_{PM} and F_{PC} are very similar. As well as using the mean of the open
 781 flux for $\delta=0$ and $\delta=34^\circ$, the value for each was employed and used to set an uncertainty
 782 on the R_X values derived.

783 The input solar wind parameters in the simulations were held constant and were
 784 solar wind speed $V_{SW}=400$ kms $^{-1}$, solar wind number density $N_{SW}=3\times 10^6$ m $^{-3}$, mean
 785 ion mass $m_{SW}=1.1$ amu, IMF flow-transverse component $B_t=5$ nT and an IMF clock
 786 angle in GSM $\theta=180^\circ$. Note that the dayside reconnection voltages of 90.8 kV and 74.3
 787 kV generated by the model are both larger than we would expect from these input so-
 788 lar wind parameters using the empirical relationship by Lockwood and McWilliams (2021a)
 789 which gives 56.1 kV for Φ_D but are more similar to the total polar cap voltage Φ_{PC} from
 790 the same study (which includes the effect of nightside reconnection and any viscous-like
 791 voltage) of 69.6 kV.

792 Figure 1 gives an indication of how dipole tilt effects influence the magnetosphere
 793 but it is not the whole story as it only shows the (XZ) plane at $Y=0$ and does not re-
 794 veal the behaviour closer to the dawn and dusk flanks. Figure 11 uses the same simu-
 795 lations to show how the total flux in the tail can be computed. It shows the magnetic
 796 field B in cross sections of the tail (YZ planes at various X) in which the minima in B
 797 clearly reveal the locations of the magnetopause currents and the cross tail current sep-
 798 arating the lobes. (Both are also clearly identified from the simulated currents). The mid-
 799 dle panel is for dipole tilt $\delta = 0$ and the two lobes are symmetrical and the cross-tail
 800 current lies at $Z=0$ at all X and Y .

801 The left-hand panel shows that for dipole tilt angle $\delta = +34^\circ$ the cross tail cur-
 802 rent sheet is warped, such that its displacement to positive Z seen at $Y=0$ in parts a
 803 and c of Figure 1 is a maximum but this displacement in Z is close to zero at the dawn
 804 and dusk flank of the tail where it connects to the magnetopause currents. It can be seen
 805 that for $\delta = +34^\circ$ the field in the southern lobe is considerably enhanced at all X com-
 806 pared to the $\delta = 0$ case, whereas in the northern hemisphere it is decreased. Because
 807 this simulation is for an geocentric dipole field, the southern hemisphere for $\delta = +34^\circ$
 808 is identical to the northern hemisphere for $\delta = -34^\circ$ (Lockwood, Owens, Barnard, Watt,
 809 et al., 2020).

810 In both cases, the field in the tail decreases with increasingly negative X . From the
 811 integral of the field threading the cross sections of the tail (the B_X component) we ob-
 812 tain the magnetic flux in each lobe at each x , $[F_{lobe}]_X$. At X below about $-20R_E$ there
 813 is no closed flux in the tail and so the decrease in this flux with increasingly negative X
 814 is only because of open flux F_X that threads the magnetopause sunward of the X in ques-
 815 tion.

816 From equation 4 we can compute the flux threading the magnetopause sunward
 817 of X , F_X and this is shown as a function of X in Figure 12a for the northern hemisphere
 818 for dipole tilt angles (positive for northern hemisphere tipped towards the Sun) of (red)
 819 $\delta = +34^\circ$, (green) $\delta = 0$ and (blue) $\delta = -34^\circ$. This plot shows that the magnitude of
 820 the effect on F_X for a hemisphere tilted towards the Sun is somewhat smaller than for

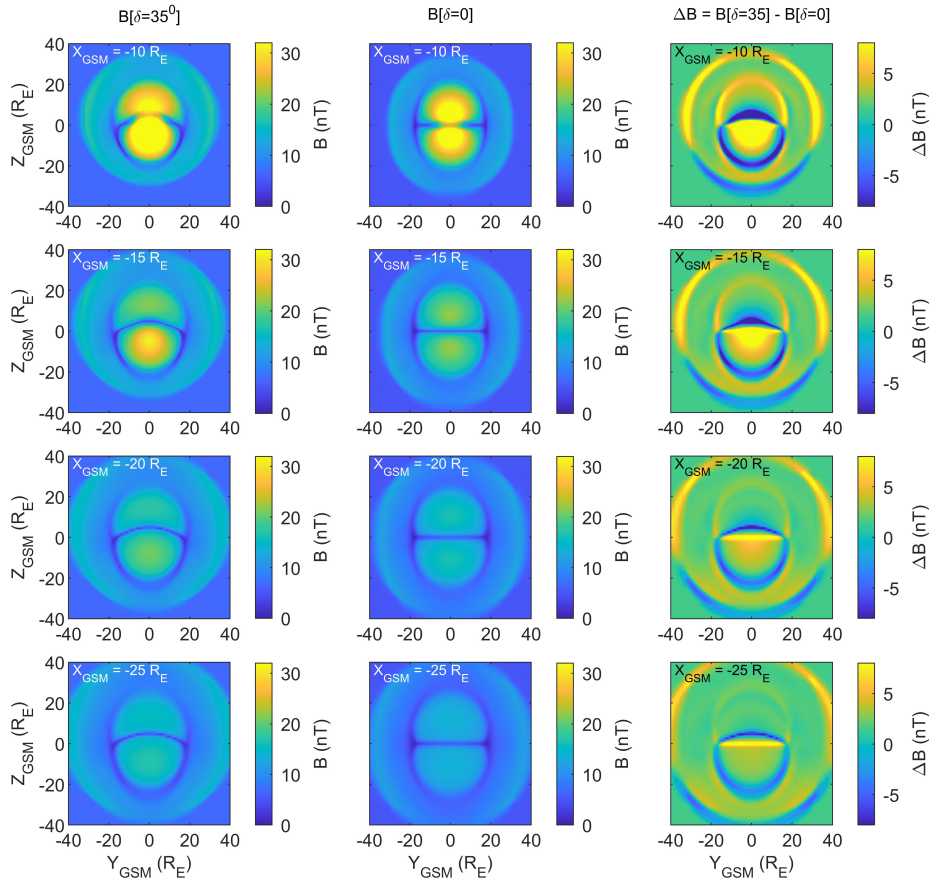


Figure 11. Cross-sections of the tail showing the field strength B in the GSM YZ plane from the simulations shown in Figure 1. From top to bottom the rows are for X of $-10R_E$, $-15R_E$, $-20R_E$, and $-25R_E$. The left-hand column is for dipole tilt angle $\delta = +34^\circ$, the middle column is for $\delta = 0$ and the right-hand column shows the difference between the two, ΔB .

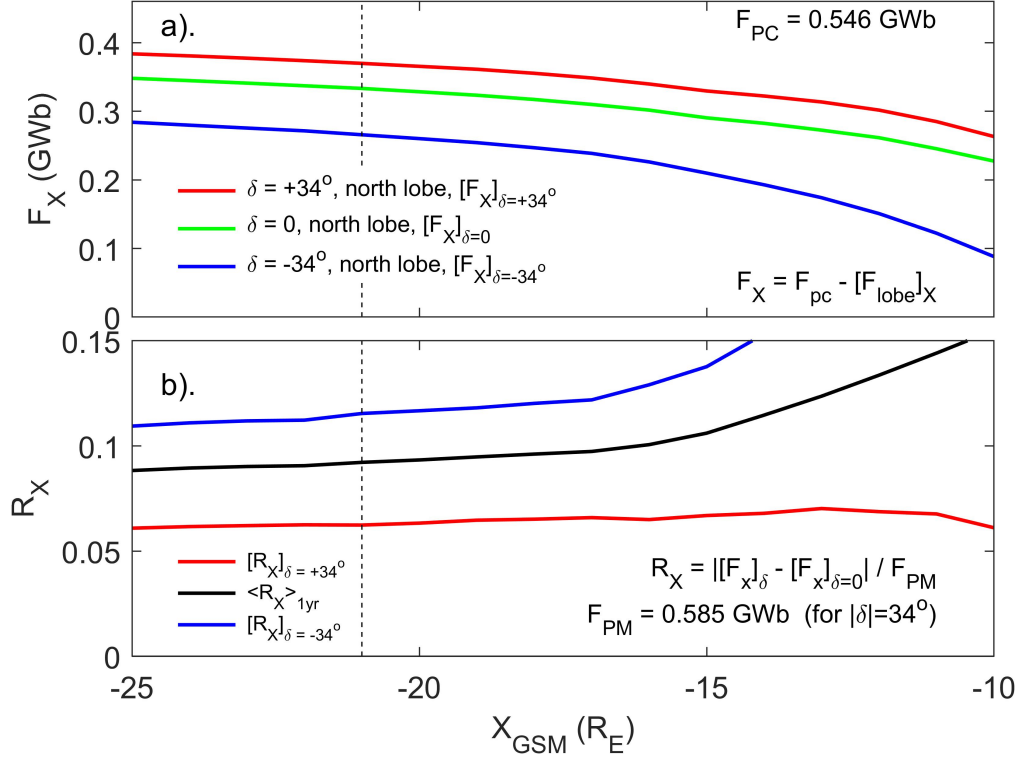


Figure 12. (a). Variation of the fluxes threading the dayside magnetopause F_X with X for a fixed polar cap flux F_{PC} of 0.546 GWb : red, green and blue are for dipole tilt angles (positive for northern hemisphere tipped towards the Sun) of $\delta = +34^\circ$, $\delta = 0$ and $\delta = -34^\circ$. The X of the tail reconnection site ($-21 R_E$) is shown by the vertical dashed line. (b) The values of R_X derived from Part a for (red) $\delta = +34^\circ$ and (blue) $\delta = -34^\circ$. The black line is the annual mean of the R_X values that are due to diurnal motions, $\langle R_X \rangle_{1\text{yr}}$, the derivation of which is explained in Figure 13.

821 a tilt of the same magnitude away from the Sun. Hence the variation in the tail is not
 822 linear with δ .

823 From these variations we can compute the R_X factors. By integration of the def-
 824 inition of R_X with time, we have:

$$R_X = (dF_X/dt)/\phi = F_X / \int \phi dt = F_X / F_{\text{PM}} = \Delta F_X / \Delta F_{\text{PM}} \quad (9)$$

825 where in this case we consider the deviation from the $\delta = 0$ case, $\Delta F_X = [F_X]_{\delta} - [F_X]_{\delta=0}$.
 826 The corresponding flux ΔF_{PM} is given by $d_{\text{PC}} \cdot B_i \cdot \Delta X$ where ΔX is the difference in the
 827 X coordinate of the diameter of the polar cap for tilt angles of δ and of $\delta = 0$. This yields
 828 $|\Delta F_{\text{PM}}|$ of 0.585 GWb for the 34° change in δ . The red lines in Figure 12b gives the val-
 829 ues of R_X for tilting the polar cap sunward from $\delta = 0$ to $\delta = +34^\circ$ (or antisunward the
 830 other way) and the blue line the value of R_X for tilting the polar cap sunward from δ
 831 $= -34^\circ$ to $\delta = 0$ (or, again, antisunward the other way). The black line gives the average
 832 over a whole year of R_X for the daily sunward/antisunward motion, $\langle R_X \rangle_{1\text{yr}}$. The deriva-
 833 tion of this from the simulation results is explained by Figure 13.

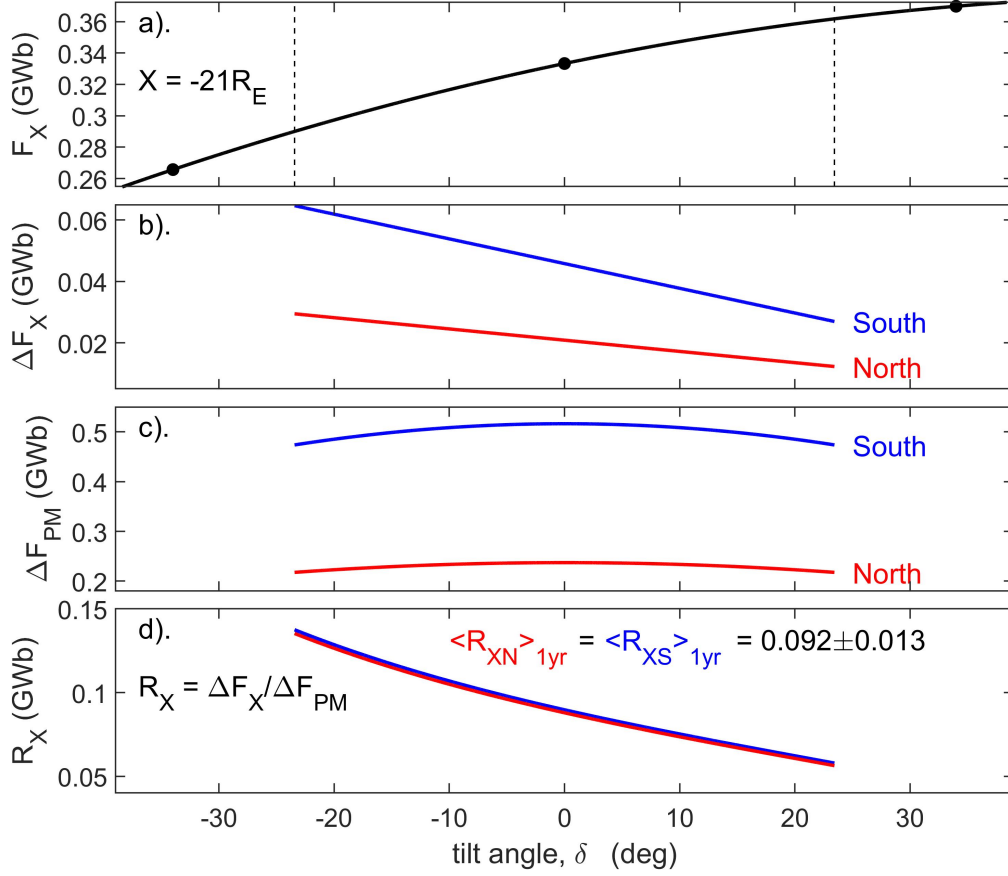


Figure 13. The derivation of the annual mean of the R_X values due to diurnal motions, $\langle R_X \rangle_{1yr}$ (the black line in Figure 12b) shown here for the example X of $-21R_E$. The points in part a are the values of the fluxes threading the dayside magnetopause F_X for $\delta = +34^\circ$, $\delta = 0$ and $\delta = -34^\circ$, as given in Figure 12a and the line is a second order polynomial fit to these points. The plot covers the full potential range of δ (for the southern pole) and the vertical dashed lines mark the range of the annual variation due to Earth's orbital motion. For each value of δ in this range the maximum and minimum δ due to the diurnal variation is considered and the change that the diurnal motions cause in F_X , ΔF_X is scaled from the polynomial fit in part a and shown in b as a function of the daily mean of δ . The corresponding change in the pole motion flux caused by the diurnal motion in the polar cap (the integral of ϕ) is calculated from Equation 1, ΔF_{PM} , and shown in Part c. Part d gives $R_X = \Delta F_X / \Delta F_{PM}$. The mean value over a whole year for both hemispheres is 0.092. An uncertainty is derived using the open flux for each of the two runs, rather than the mean of the two. This yields an uncertainty in the change that the diurnal motions cause in R_X of ± 0.013 .

834 Figure 13 is for the example X of $-21R_E$. The points in Part a are the values of
 835 the flux threading the dayside magnetopause F_X for $\delta = +34^\circ$, $\delta = 0$ and $\delta = -34^\circ$
 836 at this X , as given in Figure 12a. The line is a second order polynomial fit to these points.
 837 This has been extended out to $\pm 39^\circ$, which is the full range of possible δ values that the
 838 south pole can have. The vertical dashed lines mark the range of the annual variation
 839 due to Earth's orbital motion ($\pm 23.44^\circ$). For each value of δ between the dashed lines,
 840 the diurnal variation in δ is added and the diurnal change in F_X (ΔF_X) that it causes
 841 is then scaled from the polynomial fit in Part a and the corresponding change in the pole
 842 motion flux F_{PM} (ΔF_{PM}) (the integral of ϕ calculated from Equation 1): ΔF_X and ΔF_{PM}
 843 are shown in parts b and c, respectively, as a function of the daily mean δ , and the ra-
 844 tio of the two, (equal to R_X by Equation 9) is shown in Part d.

845 A total of 365 values of R_X were computed for the daily average of δ of each day
 846 of the year and the mean taken to give the average value over a full year caused by the
 847 diurnal variation. The results show the means are the same for the two hemispheres and
 848 equal to 0.092. The analysis was re-run using the F_{PC} of the $\delta = +34^\circ$ simulation and
 849 then again using that for $\delta = 0$ (rather than the mean of the two which is used in Fig-
 850 ures 12 and 13). This yield an uncertainty range in the R_X value of ± 0.013 .

851 The R_X value of 0.092 is of the required order of magnitude but is smaller than
 852 the 0.15 used and we need to look for potential missing factors of 1.6. There are a num-
 853 ber of considerations that can, individually or collectively, explain this factor. The val-
 854 ues of R_X depend on how much recently opened flux is present and so the time history
 855 of Φ_D is important: larger fluxes of more-recent opened field lines give a higher F_X for
 856 a given F_{PM} . The simulations are for near constant Φ_D whereas in substorm growth phases
 857 Φ_D has increased with time, giving a higher fraction F_X/F_{PC} . However, from the time
 858 variations of Φ_D shown in Figure 5, this factor gives, at most, a rise by a factor of only
 859 about 1.05 in R_X . A bigger factor is the value of the open flux F_{PC} which is only 0.546
 860 GWb in the simulations but Boakes et al. (2009) find is typically 0.75-0.9 at the time
 861 of onset. The value of F_X is close to being proportional to F_{PC} and, for a circular pol-
 862 ar cap, ϕ (and hence F_{PM}) is proportional to $F_{PC}^{0.5}$. Hence, by Equation 9, R_X is pro-
 863 portional to $F_{PC}^{0.5}$. This gives a factor of between 1.2-1.3. Another factor is the number
 864 density of the solar wind, N_{SW} which controls the magnetosheath density at the day-
 865 side magnetopause, and hence the Alfvén speed with which newly-opened field lines move
 866 over the dayside magnetopause away from the reconnection site. In the simulation, a low
 867 value was used ($3 \times 10^6 \text{ m}^3$) whereas the average value is roughly twice this. Increasing
 868 N_{SW} by a factor of 2 would lower the Alfvén speed at the dayside magnetopause by a
 869 factor of $2^{0.5} = 1.4$ and this would increase the F_X for a given F_{PC} and δ . This would
 870 therefore also increase the R_X . Lastly, the value of $R_X = 0.092$ is derived from the sim-
 871 ulations for the reconnection X-line position in those simulations at the steady state achieved
 872 at simulation time $t_s = 90$ min. As shown in Figure 1, this is at $X = -21R_E$. It is highly
 873 probable that the X-line at substorm onset forms closer to the Earth than this and Fig-
 874 ure 12 shows that the simulations give $R_X = 0.11$ at $X = -15R_E$ and $R_X = 0.12$ at X
 875 $= -13R_E$.

876 These considerations mean that the simulations can only be used as an order of mag-
 877 nitude guide but we can conclude that they give R_X values that are reasonably consis-
 878 tent with the empirically-derived value of 0.15, particularly if we take all the factors that
 879 are likely to increase the value of R_X into account.

880 6 Discussion and Conclusions

881 This paper has studied systematic UT variations in magnetospheric substorms, us-
 882 ing a simple Monte-Carlo model and 1-minute observations taken over a 34-year inter-
 883 val. In addition, a global numerical MHD model has been used to show that simulated
 884 tilt-induced changes in tail lobe flux at the tail reconnection site are of the magnitude

885 expected for this effect. Note that the MHD model used cannot reproduce the net pole-
 886 motion effect directly because it uses a geocentric rather than an eccentric dipole model.
 887 All reveal an effect consistent with the effect of diurnal motions of the magnetic poles
 888 in a geocentric-solar frame of reference caused by Earth’s rotation and the eccentric dipole
 889 nature of the intrinsic geomagnetic field.

890 The analysis has focused on the effect of dipole tilt on the tail flux as an explanation
 891 of UT effects but we should also remember that the numerical simulations give a
 892 dayside reconnection voltage Φ_D that is 16% higher (92kV) for $\delta=0$ than for $\delta=\pm 34^\circ$
 893 (78 kV). As discussed in Section 1.6 such a variation in Φ_D with δ has been invoked as
 894 the origin of the equinoctial pattern and we need to be clear what this means for aver-
 895 age variations with UT . By Maxwell’s equation $\nabla \cdot \vec{B} = 0$, Φ_D must be the same for both
 896 hemispheres (as must Φ_N) but note that transpolar voltages Φ_{PC} can differ in the two
 897 polar caps because of induction effects associated with field changes in the magnetosphere.
 898 for simplicity of explanation, we here consider a geocentric dipole (epoch 2003) and the
 899 fact that Φ_D must be the same for the two hemispheres means that the variation of Φ_D
 900 with δ must be symmetrical about zero, such that the value for a given tilt δ is the same
 901 as that for $-\delta$. The left hand column in Figure 14 shows four model variations of Φ_D
 902 with δ that meet this condition. In row (**A**) there is a minimum in Φ_D at $\delta=0$. The right
 903 hand panel shows the F - UT pattern of Φ_D (F being the fraction of a calendar year) that
 904 this generates. Averaging over all 365 days of a year at a given UT yields the means $\langle \Phi_D \rangle_F$
 905 shown as a function of UT in the middle panel the middle panel. The F - UT pattern is
 906 an “inverse equinoctial” pattern: inverse because the contours of low $|\delta|$ give minima.
 907 The variation with UT shows a semi-diurnal form with minima near 11 and 23 UT .

908 Row (**B**) shows the case for a maximum in Φ_D at $\delta=0$. This is the case that was
 909 revealed by the numerical simulations discussed in Section 5 and, indeed, the variation
 910 has been scaled to the values obtained in that section for $|\delta|=0$ and $|\delta|=\pm 34^\circ$. This does
 911 give the equinoctial pattern, with low $|\delta|$ giving maxima, as seen for geomagnetic activ-
 912 ity. The UT variation again has a semi-diurnal form, but this time it is maxima at 11
 913 hrs UT and 23 hrs UT .

914 Row (**C**) shows what happens when the peak Φ_D is at an intermediate δ (here $\pm 17.5^\circ$).
 915 The F - UT pattern is like an equinoctial form but is more complex, having a deep min-
 916 imum embedded within the bands of the maximum Φ_D . The UT variation is, however,
 917 the same in form as for (**B**).

918 The global numerical simulations by Eggington et al. (2020) are of great relevance
 919 to the present study. These authors increase the tilt angle up to the extreme limit of 90°
 920 but we here consider only the range 0 - 34° applicable to the Earth. Figure 7a of that pa-
 921 per shows that the simulated magnetopause reconnection voltage Φ_D increases with in-
 922 creased tilt angle between about 0 and 10° but thereafter decreases. Figure S2 of the Sup-
 923 porting Information file accompanying the paper shows that the open flux decreases with
 924 increased tilt angle. This means that the change in the tail reconnection voltage Φ_N is
 925 not the same as that in Φ_D and the tail voltage is independently influenced by the tilt
 926 angle, as is inferred in the present paper. The imbalance of Φ_N and Φ_D means that the
 927 magnetosphere-ionosphere system is not in steady state (Cowley & Lockwood, 1992), some-
 928 thing that can also be seen in their Figure 7b which shows unequal voltages across the
 929 northern and southern ionospheric polar caps.

930 Row (**D**) shows the results for the variation of Φ_D with δ from the simulation re-
 931 sults of Eggington et al. (2020). These have been scaled up to the same range as the other
 932 variations in the Figure. At first sight we would expect the results to be similar to those
 933 in row (**C**) for peak Φ_D at intermediate δ and indeed, the F - UT plot has similarities but
 934 the features are much narrower and sharper. This has a major effect when we average
 935 over all F and no consistent variation of $\langle \Phi_D \rangle_F$ with UT is seen. However, it should be
 936 noted that the simulations by Eggington et al. (2020) show considerable rapid time vari-

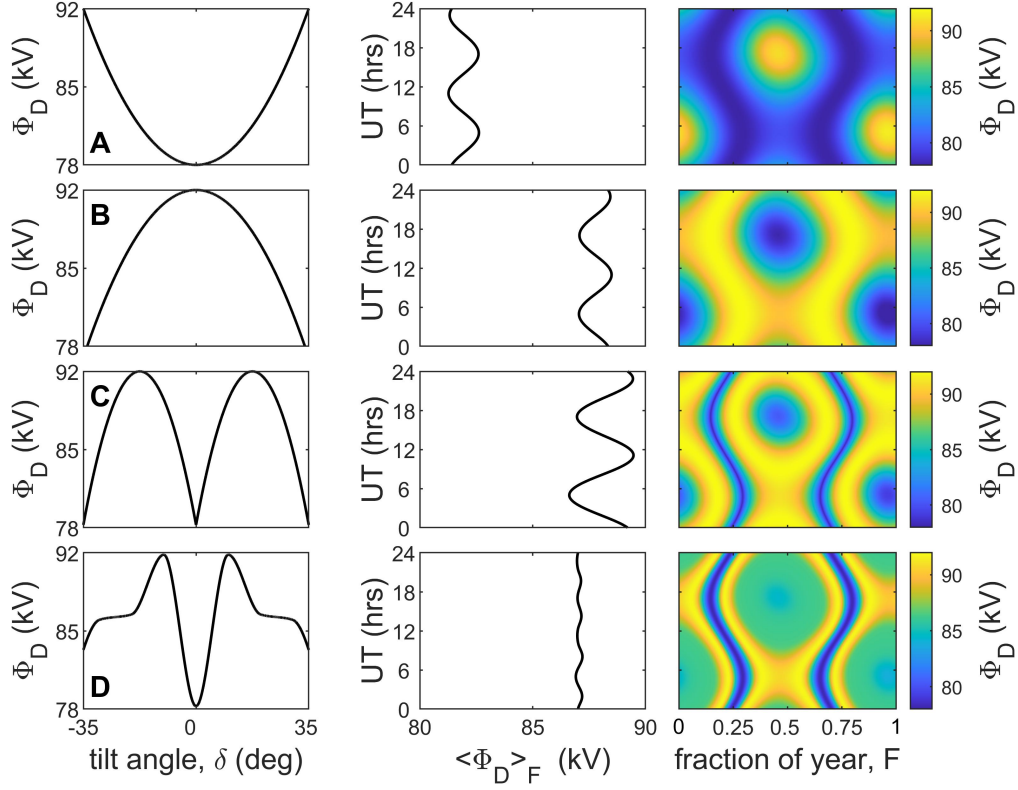


Figure 14. Analysis of the effects of various variations of the magnetopause reconnection voltage, Φ_D , with the tilt angle δ . The left-hand column gives the variation of Φ_D with δ . The right-hand column gives the resulting F - UT pattern of Φ_D (where F is the fraction of a calendar year). The middle column gives Φ_D averaged over a year (x -axis) as a function of UT (y -axis). The input variations are all scaled between a maximum of 92 kV and a minimum of 78 kV to match the results of the numerical MHD simulations shown in Figures 1, 11 and 12 and a geocentric dipole is used for simplicity. the top row (**A**) is for a minimum Φ_D at $\delta=0$; row (**B**) is for a maximum at $\delta=0$ (the variation consistent with the numerical simulation results) row (**C**) is for a maximum at $\delta=17.5^\circ$ and row (**D**) is the variation from the numerical simulations by Eggington et al. (2020) (scaled to the same minimum-to-maximum range as the other panels).

937 ation in Φ_D which the authors smooth by taking 5-minute averages with the variation
 938 indicated by error bars. This variability may have influenced the Φ_D variation with δ
 939 that is here taken from the smoothed averages and hence differences between row (**D**)
 940 and row (**C**) of Figure 14 may not be significant. Indeed the decrease in Φ_D at δ below
 941 10° may not be significant considering this numerical noise in which case the difference
 942 between rows (**D**) and (**C**) are not significant. In this case the study by Eggington et
 943 al. (2020) can be considered to give a dipole tilt dependence that could, potentially, ex-
 944 plain the equinoctial pattern through the modulation of the magnetopause reconnection
 945 voltage, Φ_D . However, as discussed earlier, a key point about these simulations is that
 946 the open flux decreases with tilt angle meaning that the reconnection voltage in the cross
 947 tail current sheet Φ_N decreases by more than the decrease in Φ_D . This points to a sec-
 948 ond, larger and independent mechanism decreasing Φ_N with increased tilt angle and ex-
 949 plaining the equinoctial pattern. This is consistent with the findings of empirical stud-
 950 ies (Finch et al., 2008; Lockwood, Owens, Barnard, Haines, et al., 2020; Lockwood, Owens,
 951 Barnard, Watt, et al., 2020) and numerical modelling studies presented here and by Lockwood,
 952 Owens, Barnard, Watt, et al. (2020).

953 Figure 14 shows that variations of Φ_D with δ can give an equinoctial pattern but
 954 the diurnal variation seen when data for a given UT are averaged over all F gives two
 955 peaks a day. These are at 10.8 hrs UT and 22.8 hrs UT for a geocentric dipole and at
 956 9.0 hrs UT and 21.0 hrs UT for an eccentric dipole (times for 2003). Figure 9 shows the
 957 dominant variation is diurnal and not semidiurnal which eliminates variations in the mag-
 958 netopause reconnection rate as the cause. That being said, the deviations from a pure
 959 sinusoidal form in Figure 9 might well be explained by a semi-diurnal oscillation in Φ_D ,
 960 but that would be a considerably smaller amplitude modulation than the dominant di-
 961 urnal one shown.

962 Another reason why we can discount the effects of modulation of Φ_D by δ for the
 963 effects studied here comes from the superposed epoch plots shown on Figure 8c. If the
 964 difference between the variations at a given UT were due to semi-diurnal variations in
 965 Φ_D , we would expect the superposed epoch variations to show oscillations in Φ_D with
 966 a 1-day period. These are not seen, but can be seen in the plots for *SML* and *SMU* (Parts
 967 a and b of Figure 8), which we would expect because of conductivity effects. We do note,
 968 however, that tilt angle effects on Φ_D could give the equinoctial pattern, but the evidence
 969 points to a larger tilt angle effect on the nightside reconnection voltage Φ_N , be it through
 970 enhanced instability in the tail to substorm onset, i.e. through lowering the tail flux thresh-
 971 old needed for onset to occur - as proposed by Kivelson and Hughes (1990), or through
 972 the effect of dipole tilt on the tail field, as modelled by Lockwood, Owens, Barnard, Watt,
 973 et al. (2020).

974 On the other hand, the paper has shown that the UT variations are consistent with
 975 the diurnal pole motions of an eccentric dipole. Using a simple Monte-Carlo model based
 976 on the idea that the probability of onset is raised by the total magnetic flux in both lobes
 977 in the near-Earth tail, we can model the observed UT variation in the number of onsets
 978 (Figure 4) except the model as yet has no way of including recurrent substorms due to
 979 persistent southward IMF and instead re-starts each growth phase at a random time.

980 This idea (of the probability of substorm onset being raised by the tail lobe field
 981 which is modulated by the dipole tilt) is supported by the superposed epoch studies. These
 982 clearly show larger magnetopause reconnection voltages are required for onsets at some
 983 UT s than at others. Figure 8 shows that the average behaviour is that after a substorm
 984 onset the reconnection voltage has fallen back to its average value in about 2 days. How-
 985 ever, before onset a considerably longer period of enhanced opening of magnetospheric
 986 flux is required. The plots (Figures 5 and 8) reveal a rise in Φ_D , on average, of order 30
 987 min ahead of an onset. This is consistent with the southward turning that traditionally
 988 starts substorm growth phases. However there seems to be two levels of precondition-
 989 ing before this. The first is an average rise in Φ_D in the 100 min prior to the southward

990 turning. The second is a preconditioning from overall average levels that increases over
991 the prior 6 days. Analysis of solar cycles shows, somewhat surprisingly, substorm onsets
992 are more common at sunspot minimum and hence this cannot be attributed to the vari-
993 ation of average solar wind conditions with the sunspot cycle.

994 A theory that allows us to accommodate the effect of pole motions and an eccen-
995 tric dipole into magnetospheric dynamics has been presented. In relation to substorm
996 growth phase termination and onsets, the **major** unknown is the extent to which dipole
997 tilts influence the tail **at the** X coordinates that influence onset. This has been allowed for
998 in the present paper with the factor R_X , which is the ratio of the change in tail lobe flux
999 at the X coordinate of the tail reconnection site to the change in total open flux in that
1000 lobe (Equations 5 and 6). The Monte-Carlo model of onsets requires $R_X \approx 0.15$, a value
1001 that is shown here to agree well with the UT variation found from the superposed epoch
1002 studies. A test of this value using a numerical MHD model of the magnetosphere is shown
1003 to result in a value near 0.10. However, there are a number of factors that could be in-
1004 voked to increase this number and make it consistent with the 0.15 value. The present
1005 paper does no more than establish that the numerical model simulations show an effect
1006 that gives the required diurnal variation with the correct phase, but the amplitude is smaller
1007 than needed to fit the observations by a factor of about a third. Further work is needed
1008 to establish if indeed $R_X=0.15$ is the correct **value. average value, and how it might vary with
solar wind and magnetospheric conditions.**

1009

References

- 1010 Alexeev, I. I., Belenkaya, E. S., Kalegaev, V. V., Feldstein, Y. I., & Grafe, A. (1996).
 1011 Magnetic storms and magnetotail currents. *Journal of Geophysical Research:*
 1012 *Space Physics*, *101*(A4), 7737–7747. Retrieved 2022-12-12, from [http://doi](http://doi.wiley.com/10.1029/95JA03509)
 1013 [.wiley.com/10.1029/95JA03509](http://doi.wiley.com/10.1029/95JA03509) doi: 10.1029/95JA03509
- 1014 Bartels, J. (1936). The eccentric dipole approximating the Earth’s magnetic
 1015 field. *Journal of Geophysical Research*, *41*(3), 225–250. Retrieved 2023-
 1016 01-20, from <http://doi.wiley.com/10.1029/TE041i003p00225> doi:
 1017 10.1029/TE041i003p00225
- 1018 Berthelier, A. (1976). Influence of the polarity of the interplanetary magnetic field
 1019 on the annual and the diurnal variations of magnetic activity. *Journal of Geo-*
 1020 *physical Research*, *81*(25), 4546–4552. Retrieved 2022-12-09, from [http://doi](http://doi.wiley.com/10.1029/JA081i025p04546)
 1021 [.wiley.com/10.1029/JA081i025p04546](http://doi.wiley.com/10.1029/JA081i025p04546) doi: 10.1029/JA081i025p04546
- 1022 Boakes, P. D., Milan, S. E., Abel, G. A., Freeman, M. P., Chisham, G., & Hubert,
 1023 B. (2009). A statistical study of the open magnetic flux content of the mag-
 1024 netosphere at the time of substorm onset. *Geophysical Research Letters*,
 1025 *36*(4), L04105. Retrieved 2022-10-23, from [http://doi.wiley.com/10.1029/](http://doi.wiley.com/10.1029/2008GL037059)
 1026 [2008GL037059](http://doi.wiley.com/10.1029/2008GL037059) doi: 10.1029/2008GL037059
- 1027 Boyle, C. B., Reiff, P. H., & Hairston, M. R. (1997). Empirical polar cap potentials.
 1028 *Journal of Geophysical Research: Space Physics*, *102*(A1), 111–125. Retrieved
 1029 2022-12-19, from <http://doi.wiley.com/10.1029/96JA01742> doi: 10.1029/
 1030 96JA01742
- 1031 Brekke, A., & Moen, J. (1993). Observations of high latitude ionospheric conduc-
 1032 tances. *Journal of Atmospheric and Terrestrial Physics*, *55*(11-12), 1493–1512.
 1033 Retrieved 2022-12-09, from [https://linkinghub.elsevier.com/retrieve/](https://linkinghub.elsevier.com/retrieve/pii/002191699390126J)
 1034 [pii/002191699390126J](https://linkinghub.elsevier.com/retrieve/pii/002191699390126J) doi: 10.1016/0021-9169(93)90126-J
- 1035 Carter, J. A., Milan, S. E., Paxton, L. J., Anderson, B. J., & Gjerloev, J. (2020).
 1036 Height-integrated ionospheric conductances parameterized by interplanetary
 1037 magnetic field and substorm phase. *Journal of Geophysical Research: Space*
 1038 *Physics*, *125*(10). Retrieved 2022-11-10, from [https://onlinelibrary.wiley](https://onlinelibrary.wiley.com/doi/10.1029/2020JA028121)
 1039 [.com/doi/10.1029/2020JA028121](https://onlinelibrary.wiley.com/doi/10.1029/2020JA028121) doi: 10.1029/2020JA028121
- 1040 Cliver, E. W., Kamide, Y., & Ling, A. G. (2000). Mountains versus valleys: Semian-
 1041 nual variation of geomagnetic activity. *Journal of Geophysical Research: Space*
 1042 *Physics*, *105*(A2), 2413–2424. Retrieved 2022-11-27, from [http://doi.wiley](http://doi.wiley.com/10.1029/1999JA900439)
 1043 [.com/10.1029/1999JA900439](http://doi.wiley.com/10.1029/1999JA900439) doi: 10.1029/1999JA900439
- 1044 Cnossen, I., Wiltberger, M., & Ouellette, J. E. (2012). The effects of seasonal
 1045 and diurnal variations in the Earth’s magnetic dipole orientation on solar
 1046 wind-magnetosphere-ionosphere coupling. *Journal of Geophysical Research:*
 1047 *Space Physics*, *117*(A11), n/a–n/a. Retrieved 2022-12-19, from [http://](http://doi.wiley.com/10.1029/2012JA017825)
 1048 doi.wiley.com/10.1029/2012JA017825 doi: 10.1029/2012JA017825
- 1049 Cowley, S. W. H., & Lockwood, M. (1992). Excitation and decay of solar wind-
 1050 driven flows in the magnetosphere-ionosphere system. *Annales Geophysicae*,
 1051 *10*, 103–115. Retrieved 2022-08-18, from [https://ui.adsabs.harvard.edu/](https://ui.adsabs.harvard.edu/abs/1992AnGeo..10..103C)
 1052 [abs/1992AnGeo..10..103C](https://ui.adsabs.harvard.edu/abs/1992AnGeo..10..103C) (ADS Bibcode: 1992AnGeo..10..103C)
- 1053 Cowley, S. W. H., Morelli, J. P., & Lockwood, M. (1991). Dependence of con-
 1054 vective flows and particle precipitation in the high-latitude dayside iono-
 1055 sphere on the X and Y components of the interplanetary magnetic field.
 1056 *Journal of Geophysical Research*, *96*(A4), 5557. Retrieved 2022-08-18, from
 1057 <http://doi.wiley.com/10.1029/90JA02063> doi: 10.1029/90JA02063
- 1058 Coxon, J. C., Milan, S. E., & Anderson, B. J. (2018, March). A review of Birkeland
 1059 current research using AMPERE. In A. Keiling, O. Marghitu, & M. Wheat-
 1060 land (Eds.), *Geophysical Monograph Series* (pp. 257–278). Hoboken, NJ, USA:
 1061 John Wiley & Sons, Inc. Retrieved 2023-04-08, from [https://onlinelibrary](https://onlinelibrary.wiley.com/doi/10.1002/9781119324522.ch16)
 1062 [.wiley.com/doi/10.1002/9781119324522.ch16](https://onlinelibrary.wiley.com/doi/10.1002/9781119324522.ch16) doi: 10.1002/9781119324522
 1063 .ch16

- 1064 Crooker, N. U., & Siscoe, G. L. (1986). On the limits of energy transfer through
 1065 dayside merging. *Journal of Geophysical Research*, *91*(A12), 13393. Retrieved
 1066 2022-12-12, from <http://doi.wiley.com/10.1029/JA091iA12p13393> doi: 10
 1067 .1029/JA091iA12p13393
- 1068 Danilov, A. A., Krymskii, G. F., & Makarov, G. A. (2013). Geomagnetic
 1069 activity as a reflection of processes in the magnetospheric tail: 1. The
 1070 source of diurnal and semiannual variations in geomagnetic activity. *Ge-*
 1071 *omagnetism and Aeronomy*, *53*(4), 441–447. Retrieved 2022-11-27,
 1072 from <http://link.springer.com/10.1134/S0016793213040051> doi:
 1073 10.1134/S0016793213040051
- 1074 de La Sayette, P., & Berthelier, A. (1996). The *am* annual-diurnal variations 1959-
 1075 1988: A 30-year evaluation. *Journal of Geophysical Research: Space Physics*,
 1076 *101*(A5), 10653–10663. Retrieved 2022-12-09, from [http://doi.wiley.com/10](http://doi.wiley.com/10.1029/96JA00165)
 1077 .1029/96JA00165 doi: 10.1029/96JA00165
- 1078 Eggington, J. W. B., Eastwood, J. P., Mejnertsen, L., Desai, R. T., & Chittenden,
 1079 J. P. (2020). Dipole tilt effect on magnetopause reconnection and the steady-
 1080 state magnetosphere-ionosphere system: Global MHD simulations. *Journal*
 1081 *of Geophysical Research: Space Physics*, *125*(7). Retrieved 2022-12-11, from
 1082 <https://onlinelibrary.wiley.com/doi/10.1029/2019JA027510> doi:
 1083 10.1029/2019JA027510
- 1084 Finch, I. D., Lockwood, M. L., & Rouillard, A. P. (2008). Effects of solar wind mag-
 1085 netosphere coupling recorded at different geomagnetic latitudes: Separation
 1086 of directly-driven and storage/release systems. *Geophysical Research Letters*,
 1087 *35*(21), L21105. Retrieved 2022-08-18, from [http://doi.wiley.com/10.1029/](http://doi.wiley.com/10.1029/2008GL035399)
 1088 2008GL035399 doi: 10.1029/2008GL035399
- 1089 Forsyth, C., Rae, I. J., Coxon, J. C., Freeman, M. P., Jackman, C. M., Gjerloev,
 1090 J., & Fazakerley, A. N. (2015). A new technique for determining Substorm
 1091 Onsets and Phases from Indices of the Electrojet (SOPHIE). *Journal of*
 1092 *Geophysical Research: Space Physics*, *120*(12), 10,592–10,606. Retrieved
 1093 2022-12-13, from <http://doi.wiley.com/10.1002/2015JA021343> doi:
 1094 10.1002/2015JA021343
- 1095 Förster, M., & Cnossen, I. (2013). Upper atmosphere differences between north-
 1096 ern and southern high latitudes: The role of magnetic field asymmetry. *Journal*
 1097 *of Geophysical Research: Space Physics*, *118*(9), 5951–5966. Retrieved 2022-
 1098 12-19, from <http://doi.wiley.com/10.1002/jgra.50554> doi: 10.1002/jgra
 1099 .50554
- 1100 Hairston, M. R., & Heelis, R. A. (1993). High-latitude electric field studies using
 1101 DMSP data. *University of Texas at Dallas, Richardson Center for Space Sci-*
 1102 *ences Report*. Retrieved 2022-12-19, from [https://apps.dtic.mil/sti/pdfs/](https://apps.dtic.mil/sti/pdfs/ADA265032.pdf)
 1103 ADA265032.pdf
- 1104 Hoilijoki, S., Souza, V. M., Walsh, B. M., Janhunen, P., & Palmroth, M. (2014).
 1105 Magnetopause reconnection and energy conversion as influenced by the dipole
 1106 tilt and the IMF B_x . *Journal of Geophysical Research: Space Physics*,
 1107 *119*(6), 4484–4494. Retrieved 2022-12-11, from [http://doi.wiley.com/](http://doi.wiley.com/10.1002/2013JA019693)
 1108 10.1002/2013JA019693 doi: 10.1002/2013JA019693
- 1109 Kabin, K., Rankin, R., Rostoker, G., Marchand, R., Rae, I. J., Ridley, A. J., ... L.,
 1110 D. D. (2004). Open-closed field line boundary position: A parametric study
 1111 using an MHD model. *Journal of Geophysical Research*, *109*(A5), A05222.
 1112 Retrieved 2022-10-27, from <http://doi.wiley.com/10.1029/2003JA010168>
 1113 doi: 10.1029/2003JA010168
- 1114 Kitamura, N., Hasegawa, H., Saito, Y., Shinohara, I., Yokota, S., Nagai, T., ...
 1115 Burch, J. L. (2016). Shift of the magnetopause reconnection line to the
 1116 winter hemisphere under southward IMF conditions: Geotail and MMS ob-
 1117 servations. *Geophysical Research Letters*, *43*(11), 5581–5588. Retrieved
 1118 2022-12-12, from <http://doi.wiley.com/10.1002/2016GL069095> doi:

- 1119 10.1002/2016GL069095
- 1120 Kivelson, M. G., & Hughes, W. J. (1990). On the threshold for triggering substorms.
- 1121 *Planetary and Space Science*, 38(2), 211–220. Retrieved 2022-11-27, from
- 1122 <https://linkinghub.elsevier.com/retrieve/pii/0032063390900855> doi:
- 1123 10.1016/0032-0633(90)90085-5
- 1124 Koochak, Z., & Fraser-Smith, A. C. (2017a). An update on the centered and
- 1125 eccentric geomagnetic dipoles and their poles for the years 1980–2015.
- 1126 *Earth and Space Science*, 4(10), 626–636. Retrieved 2022-10-27, from
- 1127 <https://onlinelibrary.wiley.com/doi/10.1002/2017EA000280> doi:
- 1128 10.1002/2017EA000280
- 1129 Koochak, Z., & Fraser-Smith, A. C. (2017b). An update on the centered and
- 1130 eccentric geomagnetic dipoles and their poles for the years 1980–2015.
- 1131 *Earth and Space Science*, 4(10), 626–636. Retrieved 2022-10-27, from
- 1132 <https://onlinelibrary.wiley.com/doi/10.1002/2017EA000280> doi:
- 1133 10.1002/2017EA000280
- 1134 Korovinskiy, D. B., Semenov, V. S., Erkaev, N. V., Ivanov, I. B., & Kiehas,
- 1135 S. A. (2018). Current sheet bending as destabilizing factor in magne-
- 1136 totail dynamics. *Physics of Plasmas*, 25(9), 092901. Retrieved 2022-
- 1137 12-11, from <http://aip.scitation.org/doi/10.1063/1.5046175> doi:
- 1138 10.1063/1.5046175
- 1139 Kubota, Y., Nagatsuma, T., Den, M., Tanaka, T., & Fujita, S. (2017). Polar cap po-
- 1140 tential saturation during the Bastille Day storm event using global MHD sim-
- 1141 ulation. *Journal of Geophysical Research: Space Physics*, 122(4), 4398–4409.
- 1142 Retrieved 2022-12-09, from <http://doi.wiley.com/10.1002/2016JA023851>
- 1143 doi: 10.1002/2016JA023851
- 1144 Kubyshkina, M., Semenov, V., Erkaev, N., Gordeev, E., & Kubyshkin, I. (2022).
- 1145 The asymmetry of magnetospheric configuration and substorms occurrence
- 1146 rate within a solar activity cycle. In A. Kostrov, N. Bobrov, E. Gordeev,
- 1147 E. Kulakov, E. Lyskova, & I. Mironova (Eds.), *Problems of Geocosmos-2020*
- 1148 (pp. 451–464). Cham: Springer International Publishing. Retrieved 2022-12-11,
- 1149 from https://link.springer.com/10.1007/978-3-030-91467-7_33 (Se-
- 1150 ries Title: Springer Proceedings in Earth and Environmental Sciences) doi:
- 1151 10.1007/978-3-030-91467-7_33
- 1152 Kubyshkina, M., Tsyganenko, N., Semenov, V., Kubyshkina, D., Partamies, N., &
- 1153 Gordeev, E. (2015). Further evidence for the role of magnetotail current shape
- 1154 in substorm initiation. *Earth, Planets and Space*, 67(1), 139. Retrieved 2022-
- 1155 12-11, from <http://www.earth-planets-space.com/content/67/1/139> doi:
- 1156 10.1186/s40623-015-0304-1
- 1157 Laitinen, T., Janhunen, P., Pulkkinen, T., Palmroth, M., & Koskinen, H. (2006).
- 1158 On the characterization of magnetic reconnection in global MHD simula-
- 1159 tions. *Annales Geophysicae*, 24(11), 3059–3069. Retrieved 2023-10-05,
- 1160 from <https://angeo.copernicus.org/articles/24/3059/2006/> doi:
- 1161 10.5194/angeo-24-3059-2006
- 1162 Laundal, K. M., Cnossen, I., Milan, S. E., Haaland, S. E., Coxon, J., Pedatella,
- 1163 N. M., ... Reistad, J. P. (2017). North-south asymmetries in Earth's mag-
- 1164 netic field: Effects on high-latitude geospace. *Space Science Reviews*, 206(1-4),
- 1165 225–257. Retrieved 2022-12-19, from <http://link.springer.com/10.1007/s11214-016-0273-0>
- 1166 doi: 10.1007/s11214-016-0273-0
- 1167 Li, H., Wang, C., & Peng, Z. (2013). Solar wind impacts on growth phase dura-
- 1168 tion and substorm intensity: A statistical approach. *Journal of Geophysical*
- 1169 *Research: Space Physics*, 118(7), 4270–4278. Retrieved 2022-12-21, from
- 1170 <http://doi.wiley.com/10.1002/jgra.50399> doi: 10.1002/jgra.50399
- 1171 Liou, K., Sotirelis, T., & Mitchell, E. (2020). Control of the east-west compo-
- 1172 nent of the Interplanetary Magnetic Field on the occurrence of magnetic sub-
- 1173 storms. *Geophysical Research Letters*, 47(5), e2020GL087406. Retrieved 2023-

- 1174 10-03, from [https://agupubs.onlinelibrary.wiley.com/doi/10.1029/](https://agupubs.onlinelibrary.wiley.com/doi/10.1029/2020GL087406)
 1175 2020GL087406 doi: 10.1029/2020GL087406
- 1176 Livermore, P., Finlay, C. C., & Bayliff, M. (2020). Recent north magnetic pole accel-
 1177 eration towards Siberia caused by flux lobe elongation. *Nature Geoscience*,
 1178 13(5), 387–391. Retrieved 2023-10-02, from [https://www.nature.com/](https://www.nature.com/articles/s41561-020-0570-9)
 1179 [articles/s41561-020-0570-9](https://www.nature.com/articles/s41561-020-0570-9) doi: 10.1038/s41561-020-0570-9
- 1180 Lockwood, M. (1991). On flow reversal boundaries and transpolar voltage in aver-
 1181 age models of high-latitude convection. *Planetary and Space Science*, 39(3),
 1182 397–409. Retrieved 2022-08-18, from [https://linkinghub.elsevier.com/](https://linkinghub.elsevier.com/retrieve/pii/003206339190002R)
 1183 [retrieve/pii/003206339190002R](https://linkinghub.elsevier.com/retrieve/pii/003206339190002R) doi: 10.1016/0032-0633(91)90002-R
- 1184 Lockwood, M. (1993). Modelling high-latitude ionosphere for time-varying
 1185 plasma convection. *IEE Proceedings H Microwaves, Antennas and Propa-*
 1186 *gation*, 140(2), 91. Retrieved 2022-08-18, from [https://digital-library](https://digital-library.theiet.org/content/journals/10.1049/ip-h-2.1993.0015)
 1187 [.theiet.org/content/journals/10.1049/ip-h-2.1993.0015](https://digital-library.theiet.org/content/journals/10.1049/ip-h-2.1993.0015) doi:
 1188 10.1049/ip-h-2.1993.0015
- 1189 Lockwood, M. (2013). Reconstruction and Prediction of Variations in the Open
 1190 Solar Magnetic Flux and Interplanetary Conditions. *Living Reviews in So-*
 1191 *lar Physics*, 10. Retrieved 2022-08-18, from [http://link.springer.com/](http://link.springer.com/10.12942/lrsp-2013-4)
 1192 [10.12942/lrsp-2013-4](http://link.springer.com/10.12942/lrsp-2013-4) doi: 10.12942/lrsp-2013-4
- 1193 Lockwood, M. (2022). Solar wind—magnetosphere coupling functions: Pitfalls,
 1194 limitations, and applications. *Space Weather*, 20(2). Retrieved 2022-05-27,
 1195 from <https://onlinelibrary.wiley.com/doi/10.1029/2021SW002989> doi:
 1196 10.1029/2021SW002989
- 1197 Lockwood, M. (2023). Northern and Southern hemisphere Polar Cap Indices: To
 1198 what extent do they agree and to what extent should they agree? *J. Geo-*
 1199 *phys. Res: Space Physics*, 128(7), e2023JA031464. Retrieved 2023-06-30, from
 1200 <https://agupubs.onlinelibrary.wiley.com/doi/10.1029/2023JA031464>
 1201 doi: 10.1029/2023JA031464
- 1202 Lockwood, M., Chambodut, A., Finch, I. D., Barnard, L. A., Owens, M. J., &
 1203 Haines, C. (2019). Time-of-day/time-of-year response functions of plane-
 1204 tary geomagnetic indices. *Journal of Space Weather and Space Climate*, 9,
 1205 A20. Retrieved 2022-08-18, from [https://www.swsc-journal.org/10.1051/](https://www.swsc-journal.org/10.1051/swsc/2019017)
 1206 [swsc/2019017](https://www.swsc-journal.org/10.1051/swsc/2019017) doi: 10.1051/swsc/2019017
- 1207 Lockwood, M., Cowley, S., Todd, H., Willis, D., & Clauer, C. (1988). Ion
 1208 flows and heating at a contracting polar-cap boundary. *Planetary and*
 1209 *Space Science*, 36(11), 1229–1253. Retrieved 2022-08-18, from [https://](https://linkinghub.elsevier.com/retrieve/pii/0032063388900761)
 1210 linkinghub.elsevier.com/retrieve/pii/0032063388900761 doi:
 1211 10.1016/0032-0633(88)90076-1
- 1212 Lockwood, M., & Cowley, S. W. H. (2022). Magnetosphere-Ionosphere Cou-
 1213 pling: Implications of Non-Equilibrium Conditions. *Frontiers in Astron-*
 1214 *omy and Space Sciences*, 9, 908571. Retrieved 2022-08-18, from [https://](https://www.frontiersin.org/articles/10.3389/fspas.2022.908571/full)
 1215 www.frontiersin.org/articles/10.3389/fspas.2022.908571/full doi:
 1216 10.3389/fspas.2022.908571
- 1217 Lockwood, M., Haines, C., Barnard, L. A., Owens, M. J., Scott, C. J., Cham-
 1218 bodut, A., & McWilliams, K. A. (2021). Semi-annual, annual and Uni-
 1219 versal Time variations in the magnetosphere and in geomagnetic activ-
 1220 ity: 4. Polar cap motions and origins of the Universal Time effect. *Jour-*
 1221 *nal of Space Weather and Space Climate*, 11, 15. Retrieved 2022-08-18,
 1222 from <https://www.swsc-journal.org/10.1051/swsc/2020077> doi:
 1223 10.1051/swsc/2020077
- 1224 Lockwood, M., Hairston, M., Finch, I. D., & Rouillard, A. P. (2009). Transpolar
 1225 voltage and polar cap flux during the substorm cycle and steady convection
 1226 events. *Journal of Geophysical Research: Space Physics*, 114(A1), n/a–n/a.
 1227 Retrieved 2022-08-18, from <http://doi.wiley.com/10.1029/2008JA013697>
 1228 doi: 10.1029/2008JA013697

- 1229 Lockwood, M., & McWilliams, K. A. (2021a). On optimum solar wind-
 1230 magnetosphere coupling functions for transpolar voltage and planetary
 1231 geomagnetic activity. *Journal of Geophysical Research: Space Physics*,
 1232 *126*(12). Retrieved 2022-05-28, from [https://onlinelibrary.wiley.com/](https://onlinelibrary.wiley.com/doi/10.1029/2021JA029946)
 1233 [doi/10.1029/2021JA029946](https://onlinelibrary.wiley.com/doi/10.1029/2021JA029946) doi: 10.1029/2021JA029946
- 1234 Lockwood, M., & McWilliams, K. A. (2021b). A survey of 25 years' transpolar volt-
 1235 age data from the SuperDARN radar network and the expanding-contracting
 1236 polar cap model. *Journal of Geophysical Research: Space Physics*, *126*(9). Re-
 1237 trieved 2022-08-18, from [https://onlinelibrary.wiley.com/doi/10.1029/](https://onlinelibrary.wiley.com/doi/10.1029/2021JA029554)
 1238 [2021JA029554](https://onlinelibrary.wiley.com/doi/10.1029/2021JA029554) doi: 10.1029/2021JA029554
- 1239 Lockwood, M., McWilliams, K. A., Owens, M. J., Barnard, L. A., Watt, C. E.,
 1240 Scott, C. J., ... Coxon, J. C. (2020). Semi-annual, annual and Universal Time
 1241 variations in the magnetosphere and in geomagnetic activity: 2. Response to
 1242 solar wind power input and relationships with solar wind dynamic pressure
 1243 and magnetospheric flux transport. *Journal of Space Weather and Space Cli-*
 1244 *mate*, *10*, 30. Retrieved 2022-08-18, from [https://www.swsc-journal.org/](https://www.swsc-journal.org/10.1051/swsc/2020033)
 1245 [10.1051/swsc/2020033](https://www.swsc-journal.org/10.1051/swsc/2020033) doi: 10.1051/swsc/2020033
- 1246 Lockwood, M., & Milan, S. (2023). Universal time variations in the magneto-
 1247 sphere. *Frontiers in Astronomy and Space Sciences*, *10*(9), 1139295. Re-
 1248 trieved 2023-02-16, from [https://www.frontiersin.org/articles/10.3389/](https://www.frontiersin.org/articles/10.3389/fspas.2023.1139295/full)
 1249 [fspas.2023.1139295/full](https://www.frontiersin.org/articles/10.3389/fspas.2023.1139295/full) doi: 10.3389/fspas.2023.1139295
- 1250 Lockwood, M., Owens, M., & Barnard, L. (2023). Universal Time variations in the
 1251 magnetosphere and the effect of CME arrival time: Analysis of the February
 1252 2022 event that led to the loss of Starlink satellites. *J. Geophys. Res. Space*
 1253 *Science*, submitted. Retrieved 2023-01-05, from [https://doi.org/10.1002/](https://doi.org/10.1002/essoar.10512909.1)
 1254 [essoar.10512909.1](https://doi.org/10.1002/essoar.10512909.1) doi: 10.1002/essoar.10512909.1
- 1255 Lockwood, M., Owens, M. J., Barnard, L. A., Haines, C., Scott, C. J., McWilliams,
 1256 K. A., & Coxon, J. C. (2020). Semi-annual, annual and Universal Time vari-
 1257 ations in the magnetosphere and in geomagnetic activity: 1. Geomagnetic
 1258 data. *Journal of Space Weather and Space Climate*, *10*, 23. Retrieved 2022-
 1259 08-18, from <https://www.swsc-journal.org/10.1051/swsc/2020023> doi:
 1260 [10.1051/swsc/2020023](https://www.swsc-journal.org/10.1051/swsc/2020023)
- 1261 Lockwood, M., Owens, M. J., Barnard, L. A., Watt, C. E., Scott, C. J., Coxon,
 1262 J. C., & McWilliams, K. A. (2020). Semi-annual, annual and Universal Time
 1263 variations in the magnetosphere and in geomagnetic activity: 3. Modelling.
 1264 *Journal of Space Weather and Space Climate*, *10*, 61. Retrieved 2022-08-
 1265 18, from <https://www.swsc-journal.org/10.1051/swsc/2020062> doi:
 1266 [10.1051/swsc/2020062](https://www.swsc-journal.org/10.1051/swsc/2020062)
- 1267 Lyatsky, W., Newell, P. T., & Hamza, A. (2001). Solar illumination as cause of
 1268 the equinoctial preference for geomagnetic activity. *Geophysical Research Let-*
 1269 *ters*, *28*(12), 2353–2356. Retrieved 2022-11-27, from [http://doi.wiley.com/](http://doi.wiley.com/10.1029/2000GL012803)
 1270 [10.1029/2000GL012803](http://doi.wiley.com/10.1029/2000GL012803) doi: 10.1029/2000GL012803
- 1271 Lyons, L. R., Zou, Y., Nishimura, Y., Gallardo-Lacourt, B., Angelopoulos, V., &
 1272 Donovan, E. F. (2018). Stormtime substorm onsets: occurrence and flow chan-
 1273 nel triggering. *Earth, Planets and Space*, *70*(1), 81. Retrieved 2022-12-19, from
 1274 [https://earth-planets-space.springeropen.com/articles/10.1186/](https://earth-planets-space.springeropen.com/articles/10.1186/s40623-018-0857-x)
 1275 [s40623-018-0857-x](https://earth-planets-space.springeropen.com/articles/10.1186/s40623-018-0857-x) doi: 10.1186/s40623-018-0857-x
- 1276 Mayaud, P.-N. (1972). The aa indices: A 100-year series characterizing the magnetic
 1277 activity. *J. Geophys. Res.*, *77*(34), 6870–6874. Retrieved from [https://doi](https://doi.org/10.1029/ja077i034p06870)
 1278 [.org/10.1029/ja077i034p06870](https://doi.org/10.1029/ja077i034p06870) doi: 10.1029/ja077i034p06870
- 1279 McIntosh, D. (1959). On the annual variation of magnetic disturbance. *Philo-*
 1280 *sophical Transactions of the Royal Society of London. Series A, Mathemati-*
 1281 *cal and Physical Sciences*, *251*(1001), 525–552. Retrieved 2022-12-09, from
 1282 <https://royalsocietypublishing.org/doi/10.1098/rsta.1959.0010> doi:
 1283 [10.1098/rsta.1959.0010](https://royalsocietypublishing.org/doi/10.1098/rsta.1959.0010)

- 1284 McWilliams, K., Pfeifer, J., & McPherron, R. (2008). Steady magnetospheric
 1285 convection selection criteria: Implications of global SuperDARN convection
 1286 measurements. *Geophysical Research Letters*, *35*(9), L09102. Retrieved
 1287 2023-10-04, from <http://doi.wiley.com/10.1029/2008GL033671> doi:
 1288 10.1029/2008GL033671
- 1289 Menvielle, M., & Berthelier, A. (1991). The *K* -derived planetary indices: Descrip-
 1290 tion and availability. *Reviews of Geophysics*, *29*(3), 415. Retrieved 2022-12-12,
 1291 from <http://doi.wiley.com/10.1029/91RG00994> doi: 10.1029/91RG00994
- 1292 Milan, S., Mooney, M., Bower, G., Fleetham, A., Vines, S., & Gjerloev, J. (2023).
 1293 Solar wind-magnetosphere coupling during hildcaas. *Journal Geophysical Re-*
 1294 *search - Space Physics, submitted.*
- 1295 Milan, S. E., Boakes, P. D., & Hubert, B. (2008). Response of the expand-
 1296 ing/contracting polar cap to weak and strong solar wind driving: Implications
 1297 for substorm onset. *Journal of Geophysical Research: Space Physics*, *113*(A9),
 1298 n/a–n/a. Retrieved 2022-10-23, from [http://doi.wiley.com/10.1029/](http://doi.wiley.com/10.1029/2008JA013340)
 1299 [2008JA013340](http://doi.wiley.com/10.1029/2008JA013340) doi: 10.1029/2008JA013340
- 1300 Milan, S. E., Carter, J. A., Sangha, H., Bower, G. E., & Anderson, B. J. (2021).
 1301 Magnetospheric flux throughput in the Dungey cycle: Identification of con-
 1302 vection state during 2010. *Journal of Geophysical Research: Space Physics*,
 1303 *126*(2), e2020JA028437. Retrieved from [https://agupubs.onlinelibrary](https://agupubs.onlinelibrary.wiley.com/doi/abs/10.1029/2020JA028437)
 1304 [.wiley.com/doi/abs/10.1029/2020JA028437](https://agupubs.onlinelibrary.wiley.com/doi/abs/10.1029/2020JA028437) doi: 10.1029/2020JA028437
- 1305 Milan, S. E., Grocott, A., & Hubert, B. (2010). A superposed epoch analysis
 1306 of auroral evolution during substorms: Local time of onset region. *Jour-*
 1307 *nal of Geophysical Research: Space Physics*, *115*(A5), n/a–n/a. Retrieved
 1308 2022-12-19, from <http://doi.wiley.com/10.1029/2010JA015663> doi:
 1309 10.1029/2010JA015663
- 1310 Milan, S. E., Walach, M., Carter, J. A., Sangha, H., & Anderson, B. J. (2019).
 1311 Substorm onset latitude and the steadiness of magnetospheric convection.
 1312 *Journal of Geophysical Research: Space Physics*, *124*(3), 1738–1752. Retrieved
 1313 2022-12-19, from [https://onlinelibrary.wiley.com/doi/abs/10.1029/](https://onlinelibrary.wiley.com/doi/abs/10.1029/2018JA025969)
 1314 [2018JA025969](https://onlinelibrary.wiley.com/doi/abs/10.1029/2018JA025969) doi: 10.1029/2018JA025969
- 1315 Mishin, V., & Karavaev, Y. (2017). Saturation of the magnetosphere dur-
 1316 ing superstorms: New results from the magnetogram inversion technique.
 1317 *Solar-Terrestrial Physics*, *3*(3), 28–36. Retrieved 2022-10-28, from [http://](http://naukaru.ru/en/nauka/article/18490/view)
 1318 naukaru.ru/en/nauka/article/18490/view doi: 10.12737/stp-33201704
- 1319 Moen, J., & Brekke, A. (1993). The solar flux influence on quiet time conductances
 1320 in the auroral ionosphere. *Geophysical Research Letters*, *20*(10), 971–974. Re-
 1321 trieved 2022-12-19, from [https://agupubs.onlinelibrary.wiley.com/doi/](https://agupubs.onlinelibrary.wiley.com/doi/abs/10.1029/92GL02109)
 1322 [abs/10.1029/92GL02109](https://agupubs.onlinelibrary.wiley.com/doi/abs/10.1029/92GL02109) doi: <https://doi.org/10.1029/92GL02109>
- 1323 Nagatsuma, T. (2004). Conductivity dependence of cross-polar potential saturation.
 1324 *Journal of Geophysical Research: Space Physics*, *109*(A4). Retrieved 2022-12-
 1325 19, from [https://agupubs.onlinelibrary.wiley.com/doi/abs/10.1029/](https://agupubs.onlinelibrary.wiley.com/doi/abs/10.1029/2003JA010286)
 1326 [2003JA010286](https://agupubs.onlinelibrary.wiley.com/doi/abs/10.1029/2003JA010286) doi: <https://doi.org/10.1029/2003JA010286>
- 1327 Newell, P. T., & Gjerloev, J. W. (2011a). Evaluation of SuperMAG auroral electro-
 1328 jet indices as indicators of substorms and auroral power. *Journal of Geophys-*
 1329 *ical Research: Space Physics*, *116*(A12), 2011JA016779. Retrieved 2022-11-06,
 1330 from <https://onlinelibrary.wiley.com/doi/10.1029/2011JA016779> doi:
 1331 10.1029/2011JA016779
- 1332 Newell, P. T., & Gjerloev, J. W. (2011b). Substorm and magnetosphere charac-
 1333 teristic scales inferred from the SuperMAG auroral electrojet indices. *Jour-*
 1334 *nal of Geophysical Research: Space Physics*, *116*(A12), 2011JA016936. Re-
 1335 trieved 2022-12-13, from [https://onlinelibrary.wiley.com/doi/10.1029/](https://onlinelibrary.wiley.com/doi/10.1029/2011JA016936)
 1336 [2011JA016936](https://onlinelibrary.wiley.com/doi/10.1029/2011JA016936) doi: 10.1029/2011JA016936
- 1337 Newell, P. T., & Gjerloev, J. W. (2012). SuperMAG-based partial ring cur-
 1338 rent indices. *Journal of Geophysical Research: Space Physics*, *117*(A5),

- 1339 2012JA017586. Retrieved 2022-12-11, from [https://onlinelibrary.wiley](https://onlinelibrary.wiley.com/doi/10.1029/2012JA017586)
 1340 [.com/doi/10.1029/2012JA017586](https://onlinelibrary.wiley.com/doi/10.1029/2012JA017586) doi: 10.1029/2012JA017586
- 1341 Newell, P. T., Sotirelis, T., Skura, J. P., Meng, C.-I., & Lyatsky, W. (2002). Ultravi-
 1342 olet insolation drives seasonal and diurnal space weather variations. *Journal of*
 1343 *Geophysical Research*, *107*(A10), 1305. Retrieved 2022-12-09, from [http://doi](http://doi.wiley.com/10.1029/2001JA000296)
 1344 [.wiley.com/10.1029/2001JA000296](http://doi.wiley.com/10.1029/2001JA000296) doi: 10.1029/2001JA000296
- 1345 Ou, J., Du, A., Ge, Y., Luo, H., Zhang, Y., & Guo, Z. (2022). Statistical study
 1346 on the North-South asymmetric distribution of the mid-low-latitude nightside
 1347 disturbed magnetic fields. *Journal of Geophysical Research: Space Physics*,
 1348 *127*(3). Retrieved 2022-12-19, from [https://onlinelibrary.wiley.com/doi/](https://onlinelibrary.wiley.com/doi/10.1029/2021JA029970)
 1349 [10.1029/2021JA029970](https://onlinelibrary.wiley.com/doi/10.1029/2021JA029970) doi: 10.1029/2021JA029970
- 1350 Park, K. S., Ogino, T., & Walker, R. J. (2006). On the importance of antiparallel
 1351 reconnection when the dipole tilt and IMF B_y are nonzero. *Journal of Geo-*
 1352 *physical Research*, *111*(A5), A05202. Retrieved 2022-12-12, from [http://doi](http://doi.wiley.com/10.1029/2004JA010972)
 1353 [.wiley.com/10.1029/2004JA010972](http://doi.wiley.com/10.1029/2004JA010972) doi: 10.1029/2004JA010972
- 1354 Pitkänen, T., Hamrin, M., Kullen, A., Maggiolo, R., Karlsson, T., Nilsson, H.,
 1355 & Norqvist, P. (2016). Response of magnetotail twisting to variations
 1356 in IMF B_y : A THEMIS case study 1–2 January 2009. *Geophysi-*
 1357 *cal Research Letters*, *43*(15), 7822–7830. Retrieved 2023-10-03, from
 1358 <https://agupubs.onlinelibrary.wiley.com/doi/10.1002/2016GL070068>
 1359 doi: 10.1002/2016GL070068
- 1360 Ridley, A. J., Gombosi, T. I., & DeZeeuw, D. L. (2004). Ionospheric control of the
 1361 magnetosphere: conductance. *Annales Geophysicae*, *22*(2), 567–584. Retrieved
 1362 2022-11-10, from <https://angeo.copernicus.org/articles/22/567/2004/>
 1363 doi: 10.5194/angeo-22-567-2004
- 1364 Russell, C. T., & McPherron, R. L. (1973). Semiannual variation of geomagnetic
 1365 activity. *Journal of Geophysical Research*, *78*(1), 92–108. Retrieved 2022-11-
 1366 03, from <http://doi.wiley.com/10.1029/JA078i001p00092> doi: 10.1029/
 1367 JA078i001p00092
- 1368 Russell, C. T., Wang, Y. L., & Raeder, J. (2003). Possible dipole tilt dependence of
 1369 dayside magnetopause reconnection. *Geophysical Research Letters*, *30*(18). Re-
 1370 trieved 2022-12-12, from <http://doi.wiley.com/10.1029/2003GL017725> doi:
 1371 10.1029/2003GL017725
- 1372 Spence, H. E. (1996). The what, where, when, and why of magnetospheric substorm
 1373 triggers. *Eos, Transactions American Geophysical Union*, *77*(9), 81–86. Re-
 1374 trieved 2022-12-19, from <http://doi.wiley.com/10.1029/96E000051> doi: 10.
 1375 1029/96E000051
- 1376 Stauning, P. (2007). A new index for the interplanetary merging electric field
 1377 and geomagnetic activity: Application of the unified polar cap indices. *Space*
 1378 *Weather*, *5*(9), n/a–n/a. Retrieved 2023-02-19, from [http://doi.wiley.com/](http://doi.wiley.com/10.1029/2007SW000311)
 1379 [10.1029/2007SW000311](http://doi.wiley.com/10.1029/2007SW000311) doi: 10.1029/2007SW000311
- 1380 Tanaka, T., Ebihara, Y., Watanabe, M., Den, M., Fujita, S., Kikuchi, T., ...
 1381 Kataoka, R. (2021). Roles of the M-I coupling and plasma sheet dissipa-
 1382 tion on the growth-phase thinning and subsequent transition to the onset.
 1383 *Journal of Geophysical Research: Space Physics*, *126*(12). Retrieved 2022-12-
 1384 19, from <https://onlinelibrary.wiley.com/doi/10.1029/2021JA029925>
 1385 doi: 10.1029/2021JA029925
- 1386 Tanskanen, E. I., Pulkkinen, T. I., Viljanen, A., Mursula, K., Partamies, N., &
 1387 Slavin, J. A. (2011). From space weather toward space climate time scales:
 1388 Substorm analysis from 1993 to 2008. *Journal of Geophysical Research: Space*
 1389 *Physics*, *116*(A5). Retrieved 2023-10-04, from [http://doi.wiley.com/](http://doi.wiley.com/10.1029/2010JA015788)
 1390 [10.1029/2010JA015788](http://doi.wiley.com/10.1029/2010JA015788) doi: 10.1029/2010JA015788
- 1391 Thébault, E., Finlay, C. C., Beggan, C. D., Alken, P., Aubert, J., Barrois, O.,
 1392 ... Zvereva, T. (2015). International Geomagnetic Reference Field: the
 1393 12th generation. *Earth, Planets and Space*, *67*(1), 79. Retrieved 2022-11-

- 1394 25, from <http://www.earth-planets-space.com/content/67/1/79> doi:
1395 10.1186/s40623-015-0228-9
- 1396 Trattner, K. J., Petrinec, S. M., Fuselier, S. A., & Phan, T. D. (2012). The lo-
1397 cation of reconnection at the magnetopause: Testing the maximum mag-
1398 netic shear model with THEMIS observations. *Journal of Geophysical Re-*
1399 *search: Space Physics*, 117(A1), 2011JA016959. Retrieved 2023-04-09, from
1400 <https://onlinelibrary.wiley.com/doi/10.1029/2011JA016959> doi:
1401 10.1029/2011JA016959
- 1402 Troshichev, O. (2022). PC index as a ground-based indicator of the solar wind
1403 energy incoming into the magnetosphere: (1) relation of PC index to the so-
1404 lar wind electric field EKL. *Frontiers in Astronomy and Space Sciences*,
1405 9, 1069470. Retrieved 2023-02-19, from [https://www.frontiersin.org/](https://www.frontiersin.org/articles/10.3389/fspas.2022.1069470/full)
1406 [articles/10.3389/fspas.2022.1069470/full](https://www.frontiersin.org/articles/10.3389/fspas.2022.1069470/full) doi: 10.3389/fspas.2022
1407 .1069470
- 1408 Tsurutani, B., Echer, E., Guarnieri, F., & Gonzalez, W. (2011). The proper-
1409 ties of two solar wind high speed streams and related geomagnetic activ-
1410 ity during the declining phase of solar cycle 23. *Journal of Atmospheric*
1411 *and Solar-Terrestrial Physics*, 73(1), 164–177. Retrieved 2023-10-04, from
1412 <https://linkinghub.elsevier.com/retrieve/pii/S1364682610001197>
1413 doi: 10.1016/j.jastp.2010.04.003
- 1414 Tulegenov, B., Raeder, J., Cramer, W. D., Ferdousi, B., Fuller-Rowell, T. J.,
1415 Maruyama, N., & Strangeway, R. J. (2023). Storm time polar cap expansion:
1416 interplanetary magnetic field clock angle dependence. *Annales Geophysicae*,
1417 41(1), 39–54. Retrieved 2023-01-20, from [https://angeo.copernicus.org/](https://angeo.copernicus.org/articles/41/39/2023/)
1418 [articles/41/39/2023/](https://angeo.copernicus.org/articles/41/39/2023/) doi: 10.5194/angeo-41-39-2023
- 1419 Tóth, G., Sokolov, I., Gombosi, T., Chesney, D., Clauer, C., De Zeeuw, D., ... Kóta,
1420 J. (2005). Space Weather Modeling Framework: A new tool for the space
1421 science community. *Journal of Geophysical Research*, 110(A12), A12226. Re-
1422 trieved 2023-10-06, from <http://doi.wiley.com/10.1029/2005JA011126> doi:
1423 10.1029/2005JA011126
- 1424 Wang, H., & Lühr, H. (2007). Seasonal-longitudinal variation of substorm occur-
1425 rence frequency: Evidence for ionospheric control. *Geophysical Research Let-*
1426 *ters*, 34(7), L07104. Retrieved 2022-11-27, from [http://doi.wiley.com/10](http://doi.wiley.com/10.1029/2007GL029423)
1427 [.1029/2007GL029423](http://doi.wiley.com/10.1029/2007GL029423) doi: 10.1029/2007GL029423
- 1428 Wang, H., Zhang, K. D., Wan, X., & Lühr, H. (2017). Universal time variation
1429 of high-latitude thermospheric disturbance wind in response to a substorm.
1430 *Journal of Geophysical Research: Space Physics*, 122(4), 4638–4653. Retrieved
1431 2022-11-27, from <http://doi.wiley.com/10.1002/2016JA023630> doi:
1432 10.1002/2016JA023630
- 1433 Zhang, B., Lotko, W., Brambles, O., Wiltberger, M., & Lyon, J. (2015). Electron
1434 precipitation models in global magnetosphere simulations. *Journal of Geo-*
1435 *physical Research: Space Physics*, 120(2), 1035–1056. Retrieved 2022-12-09,
1436 from <https://onlinelibrary.wiley.com/doi/10.1002/2014JA020615> doi:
1437 10.1002/2014JA020615
- 1438 Zhao, H., & Zong, Q.-G. (2012). Seasonal and diurnal variation of geomagnetic
1439 activity: Russell-McPherron effect during different IMF polarity and/or ex-
1440 treme solar wind conditions. *Journal of Geophysical Research: Space Physics*,
1441 117(A11), n/a–n/a. Retrieved 2022-12-29, from [http://doi.wiley.com/](http://doi.wiley.com/10.1029/2012JA017845)
1442 [10.1029/2012JA017845](http://doi.wiley.com/10.1029/2012JA017845) doi: 10.1029/2012JA017845
- 1443 Zhu, C. B., Zhang, H., Ge, Y. S., Pu, Z. Y., Liu, W. L., Wan, W. X., ... Wang,
1444 Y. F. (2015). Dipole tilt angle effect on magnetic reconnection locations on
1445 the magnetopause. *Journal of Geophysical Research: Space Physics*, 120(7),
1446 5344–5354. Retrieved 2023-04-09, from [https://onlinelibrary.wiley.com/](https://onlinelibrary.wiley.com/doi/10.1002/2015JA020989)
1447 [doi/10.1002/2015JA020989](https://onlinelibrary.wiley.com/doi/10.1002/2015JA020989) doi: 10.1002/2015JA020989
- 1448 Zou, Y., Lyons, L., Conde, M., Varney, R., Angelopoulos, V., & Mende, S. (2021).

1449 Effects of substorms on high-latitude upper thermospheric winds. *Journal*
 1450 *of Geophysical Research: Space Physics*, 126(1). Retrieved 2023-04-09, from
 1451 <https://onlinelibrary.wiley.com/doi/10.1029/2020JA028193> doi:
 1452 10.1029/2020JA028193
 1453 Østgaard, S., N.and Mende, Frey, H., Immel, T., Frank, L., Sigwarth, J., & Stubbs,
 1454 T. (2004). Interplanetary magnetic field control of the location of substorm
 1455 onset and auroral features in the conjugate hemispheres. *Journal of Geo-*
 1456 *physical Research*, 109(A7), A07204. Retrieved 2023-10-03, from [http://](http://doi.wiley.com/10.1029/2003JA010370)
 1457 [doi: 10.1029/2003JA010370](http://doi.wiley.com/10.1029/2003JA010370)

1458 7 Open Research

1459 The data used in this study are all openly available. The interplanetary data are
 1460 available from the Physics Data Facility (SPDF) at NASA’s Goddard Space Flight Cen-
 1461 ter as the Omni composite from https://omniweb.gsfc.nasa.gov/ow_min.html. The
 1462 SuperMAG SML and SMU indices and the substorm onset lists are available from the
 1463 SuperMAG project website at the Johns Hopkins University Applied Physics Labora-
 1464 tory at <http://supermag.jhuapl.edu/indices/>. The numerical MHD model results
 1465 are available from NASA’s Community Coordinated Modeling Center (CCMC) and the
 1466 simulation results are available from <https://ccmc.gsfc.nasa.gov>. The results are from
 1467 the BATSRUS global numerical model of the magnetosphere, specifically Space Weather
 1468 Modeling Framework (SWMF) version v20140611 which deploys the Rice Convection Model.
 1469 The runs employed are labelled *Henryzhou*_{040616₁}, *Henryzhou*_{040616₂}, *Henryzhou*_{040616₃}).

1470 Acknowledgments

1471 The author is grateful to the many instrument scientists and engineers who make
 1472 the datasets employed in this study possible and the staff of a number of datacentres who
 1473 allow easy access to the data: in particular the Space Physics Data Facility (SPDF) at
 1474 NASA’s Goddard Space Flight Center for the Omni composite of interplanetary obser-
 1475 vations and the SuperMAG project staff coordinated at The Johns Hopkins University
 1476 Applied Physics Laboratory, for the SMR and SML indices. The author thanks the many
 1477 PIs and instrument teams who contribute data to the SuperMAG project. The global
 1478 MHD simulation results were obtained using BATSRUS, developed by the Center for Space
 1479 Environment Modeling, at the University of Michigan with funding support from NASA
 1480 ESS, NASA ESTO-CT, NSF KDI, and DoD MURI. The author also thanks the staff on
 1481 NASA’s NASA’s Community Coordinated Modeling Center (CCMC) for making access
 1482 to and epoloitation of the model simulations possible, This work is supported by a num-
 1483 ber of grants: consolidated grants number ST/R000921/1 and ST/V000497/1 from the
 1484 United Kingdom Science and Technology Facilities Council (UKRI/STFC) and the SWIGS
 1485 Directed Highlight Topic Grant number NE/P016928/1/ and grant NE/S010033/1 from
 1486 the United Kingdom Natural Environment Research Council (UKRI/NERC).